



**HAL**  
open science

## Magnetite magnetosome biomineralization in Magnetospirillum magneticum strain AMB-1: A time course study

Lucas Le Nagard, Xiaohui Zhu, Hao Yuan, Karim Benzerara, Dennis A Bazylnski, Cecile Fradin, Adrien Besson, Sufal Swaraj, Stefan Stanescu, Rachid Belkhou, et al.

► **To cite this version:**

Lucas Le Nagard, Xiaohui Zhu, Hao Yuan, Karim Benzerara, Dennis A Bazylnski, et al.. Magnetite magnetosome biomineralization in Magnetospirillum magneticum strain AMB-1: A time course study. *Chemical Geology*, 2019, 530, pp.119348. 10.1016/j.chemgeo.2019.119348 . hal-02411165

**HAL Id: hal-02411165**

**<https://hal.science/hal-02411165>**

Submitted on 14 Dec 2019

**HAL** is a multi-disciplinary open access archive for the deposit and dissemination of scientific research documents, whether they are published or not. The documents may come from teaching and research institutions in France or abroad, or from public or private research centers.

L'archive ouverte pluridisciplinaire **HAL**, est destinée au dépôt et à la diffusion de documents scientifiques de niveau recherche, publiés ou non, émanant des établissements d'enseignement et de recherche français ou étrangers, des laboratoires publics ou privés.



1  
2  
3  
4 31 oxide speciation, from a more Fe(III)-rich species, possibly  $\alpha$ -hematite ( $\text{Fe}_2\text{O}_3$ ), to magnetite  
5  
6 32 ( $\text{Fe}_3\text{O}_4$ ), was observed in the early stages, with evidence for the presence of the Fe(III)-rich  
7  
8 33 character persisting up to 24 h. The spectromicroscopy (X-ray absorption, XAS and X-ray  
9  
10 34 magnetic circular dichroism, XMCD) and TEM results show that biomineralization occurs in a  
11  
12 35 stepwise fashion. First, very small particles, with no measurable magnetization, are produced at  
13  
14 36 different sites in the cell without significant chain formation. The Fe  $L_3$  spectra of these early  
15  
16 37 stage particles typically differ from magnetite with an additional signal at 708.4 eV that is  
17  
18 38 consistent with  $\alpha$ -hematite. By 6-8 h the particles are more numerous, partial chain formation is  
19  
20 39 evident, and the  $L_3$  spectrum is very similar to that of magnetite. By 24 h particles-in-chains are  
21  
22 40 the dominant motif and magnetism with the moment along the chain is established. By 48 h the  
23  
24 41 cells are essentially the same as cells grown in Fe-rich medium.

25  
26 43 **Keywords:** magnetotactic bacteria; *Magnetospirillum magneticum* strain AMB-1;  
27  
28 44 biomineralization; time course; transmission electron microscopy; synchrotron  
29  
30 45 spectro-microscopy; STXM; X-ray absorption; X-ray magnetic circular dichroism

31  
32 47 **Highlights:**

- 33 48 \* TEM and STXM study of magnetosome biomineralization in AMB-1 magnetotactic bacteria  
34 49 \* time course method: cells cultured without Fe; placed in normal medium; sampled at 0.15, 0.5,  
35 50 1, 2, 4, 5.7, 8, 12, 24, 28 h  
36  
37 51 \* TEM particle counts/cell; STXM measure Fe L X-ray absorption and X-ray magnetic circular  
38 52 dichroism  
39  
40 53 \* Fe(III) rich precursor, possibly  $\alpha$ -hematite, observed in <8 h samples  
41 54 \* pure magnetite particles aligned in chains form by 12 hr; gaps and magnetic reversals persist at  
42 55 48 h

43  
44  
45  
46 58 Chemical Geology (submitted 19 June 2019; REVISION submitted 13 Sep 2019; final sun 19-Oct 20119)

47  
48  
49 60 File: AMB-1-time-course-STXM-revised2.doc

50  
51 62 **Last changed: 19 Oct 2019**

52  
53 64 <sup>+</sup> present address: School of Physics & Astronomy, The University of Edinburgh, Scotland

54  
55 66 # present address: School of Environmental and Chemical Engineering, Shanghai University,  
56  
57 67 200444, Shanghai, China.

58  
59 68 \* corresponding author. Email: [aph@mcmaster.ca](mailto:aph@mcmaster.ca)

1  
2  
3  
4 69  
5 70 **1. Introduction**  
6

7 71 Magnetotactic bacteria (MTB) biomineralize intracellular, single-magnetic-domain,  
8  
9 72 single-crystal, membrane- bounded magnetite ( $\text{Fe}_3\text{O}_4$ ) or greigite ( $\text{Fe}_3\text{S}_4$ ) nanoparticles known as  
10  
11 73 magnetosomes (Bazylinski and Frankel 1995). Magnetosomes are generally organized as a chain  
12  
13 74 or chains within the cell (Bazylinski 1999). In this arrangement, they function as a strong  
14  
15 75 magnetic dipole, so the cell passively aligns along the Earth's geomagnetic field lines like a  
16  
17 76 compass needle. Coupled with aerotaxis (chemotaxis to the concentration of  $\text{O}_2$ ),  
18  
19 77 magneto-aerotaxis is believed to increase the efficiency of MTB in locating and maintaining  
20  
21 78 their position at their optimal  $\text{O}_2$  concentration and redox poise for survival in sediments or  
22  
23 79 stratified water columns (Bazylinski 1999). The optimal  $\text{O}_2$  concentration/redox conditions for  
24  
25 80 most MTB appears to be at, or close to, the oxic-anoxic interface (OAI) (Faivre & Schuler 2008).  
26  
27 81 MTB, which likely evolved in the mid-Archaeon, are of tremendous interest as possibly one of  
28  
29 82 the earliest organisms on Earth capable of magnetic sensing and biomineralization (Lin *et al.*  
30  
31 83 2017). They are a superb 'laboratory' for dissecting controlled biomineralization. They  
32  
33 84 significantly impact the magnetic properties of sediments (Chen *et al.* 2015), and are implicated  
34  
35 85 in the geochemical cycles of phosphorus (Rivas *et al.* 2018, Schulz-Vogt *et al.* 2019) and iron  
36  
37 86 (Lin et al 2013, Lin et al 2014, Chen *et al.* 2014, Amor et al 2019). Through measurements of the  
38  
39 87 iron content of single AMB-1 cells, Amor et al (2019) showed that MTB absorb a significant  
40  
41 88 fraction of the iron dissolved in their environment and thus play an important role in global iron  
42  
43 89 distributions. Cells of a mutant lacking core genes for biomineralization also contained a  
44  
45 90 significant (but decreased) amount of iron, indicating that magnetosomes are only one reservoir  
46  
47 91 of iron among others in MTB.  
48

49  
50  
51 92 The genetic control of magnetosome biomineralization is an active area of study. A  
52  
53 93 conserved core of essential genes has been identified (Komeili *et al.* 2004, Jogler and Schuler,  
54  
55 94 2007, Arakaki *et al.* 2008, Murat *et al.* 2012). However, the chemical steps and reactions in  
56  
57 95 magnetosome biomineralization are still not fully understood (Lefevre & Bazylinski, 2013).  
58  
59 96 Several competing hypotheses exist. Frankel *et al.* (1983) reported that  $(\text{Fe}^{3+})_2\text{O}_3 \cdot 0.5\text{H}_2\text{O}$ , an  
60  
61  
62  
63  
64  
65

1  
2  
3  
4  
5 97 amorphous ferrihydrite, is formed first, and is then partially reduced and dehydrated to Fe<sub>3</sub>O<sub>4</sub>.  
6  
7 98 Faivre *et al.* (2007) did not observe any well-ordered, crystalline precursors in a time-resolved  
8  
9 99 Mössbauer study. They found that Fe<sup>2+</sup> or Fe<sup>3+</sup> was taken into the cell and converted into an  
10  
11 100 intracellular amorphous ferrous high-spin species, predominantly located in the magnetosome  
12  
13 101 membrane, along with ferritin. These then quickly co-precipitate to directly form Fe<sub>3</sub>O<sub>4</sub> within  
14  
15 102 magnetosome vesicles. In a recent ptychography study, Zhu *et al.* (2016) observed hematite  
16  
17 103 ( $\alpha$ -Fe<sub>2</sub>O<sub>3</sub>) in cells of *Magnetovibrio blakemorei* strain MV-1 which was interpreted to be a  
18  
19 104 possible precursor to magnetite in the formation of magnetite magnetosomes.

20  
21 105 Results from various time course studies of magnetite magnetosome synthesis in MTB are  
22  
23 106 summarized in **Supplemental Information Table S-1**. These studies all focused on either  
24  
25 107 *Magnetospirillum magneticum* strain AMB-1 or *Magnetospirillum gryphiswaldense* strain  
26  
27 108 MSR-1 as the model MTB for magnetite biomineralization. With some exceptions, there seems  
28  
29 109 to be a general consensus that:

30  
31 110 \* a lag phase occurs before particle formation, typically in the 0.5-2 hour (h) range (Li *et al.*  
32  
33 111 2009).

34  
35 112 \* crystal growth occurs in lipid bilayer membrane vesicles which are present prior to the  
36  
37 113 visible detection of crystals (Komeli *et al.* 2004).

38  
39 114 \* there is a period of time during which the mean size of the particles is in the  
40  
41 115 superparamagnetic size range, significantly smaller than that of mature magnetosomes, and  
42  
43 116 there is a broad size distribution (Firlar *et al.* 2016).

44  
45 117 \* the particles are poorly organized in the early stages of biomineralization but become  
46  
47 118 arranged in chains with more or less regular spacing, after a period of time which varies  
48  
49 119 considerably depending on the study (Heyen and Schüler 2003, Firlar *et al.* 2016), suggesting  
50  
51 120 that the temporal evolution depends on the culturing and growth conditions (growth phase,  
52  
53 121 O<sub>2</sub> concentration, temperature, etc).

1  
2  
3  
4  
5  
6  
7  
8  
9  
10  
11  
12  
13  
14  
15  
16  
17  
18  
19  
20  
21  
22  
23  
24  
25  
26  
27  
28  
29  
30  
31  
32  
33  
34  
35  
36  
37  
38  
39  
40  
41  
42  
43  
44  
45  
46  
47  
48  
49  
50  
51  
52  
53  
54  
55  
56  
57  
58  
59  
60  
61  
62  
63  
64  
65

\* after 24-48 h, the size and shape of individual particles and their organization in the cell approach that in magnetosomes present in stationary phase MTB grown with a major source of Fe.

\* the magnetic properties of particles produced in the early stages differ greatly. Staniland *et al.* (2007), using ensemble averaged Fe L-edge X-ray magnetic circular dichroism (XMCD), stated that a full XMCD response, and thus magnetic magnetite, was detected 15 minutes (m) after Fe-depleted cells were placed in a standard growth medium containing a major source of Fe. However, Faivre *et al.* (2007) only detected Mössbauer signal indicative of magnetite 95 m after incubation with iron. Similarly, Baumgartner *et al.* (2013), using magnetically induced differential light scattering, only found a magnetic response 80 m after incubation with Fe. Baumgartner *et al.* (2013) also used ensemble averaged X-ray absorption spectroscopy (XAS) to show that Fe K-edge features typical of magnetite only appeared after ~100 m, consistent with their magnetic measurements. Li *et al.* (2009), using temperature-dependent magnetometry, detected a magnetic response characteristic of magnetite (hysteresis and Verwey transition) 28 h after the start of the time course, which, unfortunately, was their first time data point. We note that the variation in magnetic results may simply reflect the use of different methods which have different spatial, concentration and magnetic field sensitivities.

\* there is an Fe(III)-rich intermediate to magnetite. While the presence of some type of Fe(III) in cells in the early stages of growth is a common observation, there is disagreement whether this is a single mineral precursor species with a unique chemical composition and structure, a mixture of species, or simply Fe(III) ions. Some report such precursors to be amorphous, others as crystalline. In some cases, this is reported as a surface  $\alpha$ -hematite layer (Staniland *et al.* 2007, Firlar *et al.* 2019). Using XAS, Fdez-Gubieda *et al.* (2013) identified phosphorus-rich ferrihydrite as a precursor of magnetite in MSR-1 but were unable to image the precursors with high resolution transmission electron microscopy (TEM). Using K-edge XAS and extended X-ray absorption fine structure (EXAFS) and a more complete set of

1  
2  
3  
4  
5  
6  
7  
8  
9  
10  
11  
12  
13  
14  
15  
16  
17  
18  
19  
20  
21  
22  
23  
24  
25  
26  
27  
28  
29  
30  
31  
32  
33  
34  
35  
36  
37  
38  
39  
40  
41  
42  
43  
44  
45  
46  
47  
48  
49  
50  
51  
52  
53  
54  
55  
56  
57  
58  
59  
60  
61  
62  
63  
64  
65

reference spectra, Baumgartner *et al.* (2013) concluded from spectra similar to those measured by Fdez-Gubieda *et al.* (2013) that a disordered ferric phosphate-like phase forms at the beginning of the time-course, which is quickly (< 30 m) converted into magnetite. Very recently, Wen *et al.* (2019) reported electron diffraction evidence of very small crystals of  $\epsilon$ -Fe<sub>2</sub>O<sub>3</sub> in the very early stages of their time course study of MSR-1. The lack of consistency in this aspect of the biomineralization is, at least in part, due to the use of different analytical methods, each with a specific sampling depth, spatial resolution, chemical sensitivity, and structural sensitivity.

Marcano *et al.* (2017) recently reported results from a time-course experiment which showed that the cell growth phase (lag vs. exponential vs. stationary) at the time of Fe-induction had an influence on the magnetite biomineralization process in *M. gryphiswaldense* strain MSR-1. They showed that magnetosome particle synthesis is initially slow but eventually leads to the production of larger particles and a higher cellular magnetite content for iron-depleted cultures where cells are in the exponential phase at the time of iron-induction, compared to those in the arrested growth state. This dependence on specific experimental conditions could explain the apparent lack of consistency in the results from previous time course studies.

Although numerous efforts have been made to reveal the mechanism of magnetosome biomineralization inside MTB cells, several critical questions still need to be addressed: *Are there mineral (other than magnetite) precursors formed before magnetite magnetosome formation? If they exist, can we identify and locate these precursors? How are different precursor species and/or Fe ions inside magnetosome vesicles converted to magnetite, Fe<sub>3</sub>O<sub>4</sub>? How do they become organized into chains with aligned magnetic moments?*

One approach to address these issues is to use spatially resolved methods to characterize the chemical and magnetic properties of MTB on an individual cell and individual particle basis throughout the process of biomineralization. Here we report results of a time course study of the biomineralization of magnetite magnetosomes in *Magnetospirillum magneticum* strain AMB-1. We used X-ray absorption spectroscopy (XAS) and XMCD measured at the Fe L<sub>3</sub>-edge by

1  
2  
3  
4  
5 176 scanning transmission X-ray microscopy (STXM) to characterize cellular interior and individual  
6  
7 177 magnetosomes in cells at various time points after initiation of biomineralization. XAS can  
8  
9 178 identify different Fe species and thus identify precursor particles and possibly soluble Fe species  
10  
11 179 (Zhu *et al.* 2016). XAS and XMCD can be used to monitor how the ratio of Fe(II) to Fe(III)  
12  
13 180 changes as the biomineralization of Fe<sub>3</sub>O<sub>4</sub> proceeds. The power of our approach over most  
14  
15 181 earlier time course studies is the ability to examine and spectroscopically analyze individual  
16  
17 182 particles within a single cell. Our strategy was to start with cells grown in the absence of Fe  
18  
19 183 which do not contain magnetosomes, and then to initiate magnetosome biomineralization by  
20  
21 184 inoculating these cells into standard Fe-containing culture medium. We then sampled at various  
22  
23 185 times during a 48 h period after the start of the time course, and subsequently measured TEM  
24  
25 186 and STXM from those samples in order to investigate magnetosome biomineralization and chain  
26  
27 187 formation over time.

## 28 29 188 30 189 31 32 190 **2. Experimental**

### 33 191 34 35 192 *2.1 Sample preparation*

36  
37 193 Cells of *M. magneticum* strain AMB-1 were initially grown in a Fe-rich liquid medium  
38  
39 194 under controlled microaerobic conditions with 1.5% O<sub>2</sub> in the headspace of the culture, as  
40  
41 195 previously described (Le Nagard *et al.* 2018). The growth medium contained, per liter: 1.0 mL  
42  
43 196 modified Wolfe's mineral elixir (Wolin *et al.*, 1963, Bazylinski *et al.*, 2000), 0.1 g KH<sub>2</sub>PO<sub>4</sub>, 0.15  
44  
45 197 g MgSO<sub>4</sub>·7H<sub>2</sub>O, 2.38 g (4-(2-hydroxyethyl)-1-piperazineethanesulfonic acid (HEPES buffer),  
46  
47 198 0.34 g NaNO<sub>3</sub>, 0.1 g yeast extract (BD 210929), 3.0 g Becton Dickinson (BD) Bacto™ Soytone  
48  
49 199 (BD 243620), 4.35 mL potassium lactate (60% solution) and 5 mL Fe (III) citrate 10 mM stock  
50  
51 200 solution.

52  
53 201 Several weeks prior to starting a time course experiment, cells were grown in a Fe-depleted  
54  
55 202 liquid growth medium similar to the Fe-rich growth medium except that the amount of BD  
56  
57 203 Bacto™ Soytone was reduced to 1.0 g/L and the Fe(III) citrate and mineral solutions and the  
58  
59 204 yeast extract were omitted. For the first set of samples (batch A, November 2017), cells were



1  
2  
3  
4  
5 205 grown in the Fe-depleted medium with 5% O<sub>2</sub> in the headspace. The increased O<sub>2</sub> concentration  
6  
7 206 led to a quicker decrease in the number of magnetosomes per cell compared to cultures grown in  
8  
9 207 Fe-depleted conditions with 1.5% O<sub>2</sub> in the headspace. It took 5 successive inoculations into  
10  
11 208 fresh, Fe-depleted medium over a 2-week period to achieve cultures in which standard measures  
12  
13 209 of a magnetic population – hanging drop and reflectivity modulation over a magnetic stirrer –  
14  
15 210 indicated that most cells had lost their magnetism. In addition, transmission electron microscopy  
16  
17 211 (TEM) showed most cells did not contain particles, although some had 1 or 2 particles. For batch  
18  
19 212 B, the O<sub>2</sub> concentration in the headspace was increased to 20%, which caused cells in the culture  
20  
21 213 to grow more vigorously, and to become non-magnetic even more quickly than at 5% O<sub>2</sub>.  
22  
23 214 Respectively, >10 and 7 stages of depletion were performed for the batch A and B samples. At  
24  
25 215 each stage, 1 mL of the (n-1) stage culture was inoculated into 60 mL of fresh Fe-depleted  
26  
27 216 medium and incubated at 32 °C for 3-4 days in order to reach the stationary phase, before  
28  
29 217 performing the next transfer. The magnetism of the culture was assessed at each stage using the  
30  
31 218 hanging drop test, in which the response of the cells to an external magnetic field is studied using  
32  
33 219 optical microscopy (Le Nagard *et al.*, 2018b). TEM was also used to estimate the number of  
34  
35 220 particles per cell. For both batch A and batch B, there was no observable change in the hanging  
36  
37 221 drop test and in TEM analysis results after 5-6 depletion stages.

38  
39  
40 222 The time course experiment was initiated by inoculating 30 mL of the Fe-depleted culture  
41  
42 223 into 30 mL of the Fe-rich medium under anaerobic conditions. O<sub>2</sub> was immediately added to the  
43  
44 224 culture after inoculation to obtain a concentration of 1.5% O<sub>2</sub> in the headspace of the culture.  
45  
46 225 Samples were then removed from the culture at intervals of 0, 10, and 30 min (m) and 1, 2, 4,  
47  
48 226 5.7, 8, 12, 24, and 48 hours (h). Immediately after collecting a culture sample, the extracted  
49  
50 227 aliquot was placed into a centrifuge vial and heated at 60 °C for 10 m to kill the cells and stop  
51  
52 228 magnetosome biomineralization (Cazares *et al.* 2015). These samples were then stored at 4 °C  
53  
54 229 until they were prepared for TEM and STXM.

55  
56 230 For the batch A samples, ~2 µl were drop cast on to formvar coated 3 mm TEM grids. A  
57  
58 231 washing step was not applied, and as a consequence, most of the cells were encrusted with  
59  
60  
61  
62  
63  
64  
65

1  
2  
3  
4  
5 232 residual salts from the culture medium. For the batch B samples, 3 different sample mounting  
6  
7 233 approaches were used. Immediately after heat sterilizing the cells at each time point during the  
8  
9 234 time course, about 2  $\mu$ l were drop cast on to C-flat 3 mm TEM grids  
10  
11 235 (<https://www.protochips.com/products/c-flat/>). After investigation by TEM it was found that  
12  
13 236 there were still some residual salts (but much less than in the batch A samples) so a new set of  
14  
15 237 batch B samples for STXM was prepared using glutaraldehyde fixation (Chao & Zhang 2011)  
16  
17 238 followed by multiple washings in distilled deionized water and centrifuge separations. This has  
18  
19 239 been shown to result in samples free of salt precipitates, with cells retaining the particles in their  
20  
21 240 as-grown state (Le Nagard *et al* 2018a). The glutaraldehyde-fixed material was drop cast on  
22  
23 241 silicon nitride windows (Norcada) and formvar coated TEM grids.  
24  
25 242

## 26 243 *2.2 Scanning Transmission X-ray microscopy (STXM)*

27  
28  
29 244 STXM analyses were performed at HERMES, the soft X-ray spectromicroscopy beamline at  
30  
31 245 SOLEIL (St. Aubin, France) (Belkhou *et al*, 2015, Swaraj *et al.*, 2017). STXM methodology has  
32  
33 246 been described in detail previously (Hitchcock 2012, Hitchcock 2015). Briefly, monochromated  
34  
35 247 X-rays are focused to a  $\sim$ 30 nm spot by a Fresnel zone plate. The sample is positioned at the  
36  
37 248 focal point and x-y raster scanned while recording the intensity of the transmitted X-rays. After  
38  
39 249 locating cells of interest, aided by optical imaging and, in some cases, TEM, STXM images were  
40  
41 250 measured at a sequence of photon energies (a stack). In all cases, the region measured contained  
42  
43 251 a suitable area free of cells to measure the incident flux ( $I_0$ ), which is needed to convert  
44  
45 252 transmitted intensities to optical density (OD). Circular right (CR) polarized light was used  
46  
47 253 without any applied magnetic field. For some samples measurements were performed with both  
48  
49 254 helicities – i.e. both circular left (CR) and circular right (CL) polarized light. XMCD maps were  
50  
51 255 then generated from the difference of OD-converted CR- and CL-images at 708.2 eV - the  
52  
53 256 energy of strongest X-ray magnetic circular dichroism (XMCD) signal for magnetite (Goering *et*  
54  
55 257 *al.* 2007, Zhu *et al.* 2015). XMCD spectra are the (CR – CL) difference, recorded at all energies  
56  
57 258 across the Fe  $L_3$  edge. STXM studies of the batch A samples were performed in November 2017  
58  
59 259 with the sample tilted at 32° relative to the focal plane. For the batch B samples, XAS and  
60  
61

1  
2  
3  
4  
5 260 XMCD were measured in December 2018, using both 0° tilt (X-ray beam direction normal to the  
6  
7 261 sample plane) and 30° tilt (sample grid tilted at 30° relative to the focal plane).

8  
9 262

### 10 263 *2.3 Data analysis – STXM, XAS & XMCD*

11  
12 264 Most of the results were obtained using XAS stacks - a set of images measured over a  
13  
14 265 sequence of photon energies in the Fe L<sub>3</sub> region (700 – 717 eV). After image alignment and  
15  
16 266 conversion of the transmission signal to OD, the many-energy stacks were further processed by  
17  
18 267 extracting internal reference spectra from unique morphologies such as the particles and the  
19  
20 268 cytoplasm, then fitting the stack to those reference spectra in order to generate component maps.  
21  
22 269 In some cases, the component maps are presented as color coded composites in which the signal  
23  
24 270 of each component is scaled to fill its color scale (so called rescaled, rather than absolute color  
25  
26 271 composites) (Hitchcock, 2012). In cases where both CR and CL multi-energy stacks were  
27  
28 272 acquired, these were combined into a single file prior to alignment and OD conversion, and then  
29  
30 273 separated to allow generation of XMCD stacks from the difference (CR-CL) which allowed  
31  
32 274 extraction of the magnetic signal from individual particles. All STXM data analysis was  
33  
34 275 performed using aXis2000 (<http://unicorn.mcmaster.ca/aXis2000.html>).

35  
36  
37 276 In this work, in contrast to typical XMCD measurements in materials science, the intrinsic  
38  
39 277 magnetic properties of a sample are measured without using any applied magnetic field. There  
40  
41 278 are strict geometric requirements to measure magnetization by XMCD. As outlined in **Fig. 1**, the  
42  
43 279 magnitude of the XMCD signal is determined by the dot product of the magnetization vector of  
44  
45 280 the sample and the polarization vector of the photon. The polarization vector of circularly  
46  
47 281 polarized photons points either forward (CR) or backward (CL) along the X-ray propagation  
48  
49 282 direction. In order to have a measurable XMCD signal there must be a non-zero projection of the  
50  
51 283 magnetization vector of the sample along the photon polarization. The magnetization vector of  
52  
53 284 chains of magnetosomes in magnetotactic bacteria grown in high-Fe culture is typically along the  
54  
55 285 cell axis. Thus, a cell lying flat on its support should be positioned such that the long axis of the  
56  
57 286 cell is horizontal and the sample is tilted out of the plane normal to the X-ray propagation  
58  
59 287 direction. We typically use a polar tilt angle of ~30° for which the projection of an in-plane,

1  
2  
3  
4  
5  
6  
7  
8  
9  
10  
11  
12  
13  
14  
15  
16  
17  
18  
19  
20  
21  
22  
23  
24  
25  
26  
27  
28  
29  
30  
31  
32  
33  
34  
35  
36  
37  
38  
39  
40  
41  
42  
43  
44  
45  
46  
47  
48  
49  
50  
51  
52  
53  
54  
55  
56  
57  
58  
59  
60  
61  
62  
63  
64  
65

288 horizontally oriented magnetic moment is 50%. Since monitoring the development of the chains  
289 and their magnetic alignment is the goal of this project, we have made measurements at both 0°  
290 and 30° tilt angles. Any XMCD signal detected with the sample at a tilt angle of 0° indicates  
291 there is an out-of plane component to the magnetization (i.e. a component orthogonal to the grid  
292 on which the cell is deposited).

#### 294 *2.4 Data analysis –particle size distributions from statistical evaluation of TEM images*

295 The average number of particles and their typical size in cells of the glutaraldehyde-fixed  
296 Batch B samples were determined by TEM. Individual cells were randomly selected on the grids  
297 and imaged at 40,000x – 60,000x magnification. This study was performed after the STXM  
298 measurements, to avoid damaging the samples with high magnification TEM. 20 cells were  
299 imaged per sample, and a minimum of N=18 cells in each sample were subjected to detailed  
300 image analysis. Particles were counted and measured manually. Large variations in the contrast  
301 of the particles (size dependency and inhomogeneous background) made it difficult to use an  
302 automated procedure. The oval selection tool of the ImageJ software was used to draw a shape  
303 that best matched the projection of each particle in the focal plane. The surface area of that  
304 projection was measured and converted to a diameter, assuming the particles to be spherical.  
305 There is significant uncertainty in the measurement of particles smaller than 10 nm, due to  
306 insufficient spatial resolution at the magnifications used in this study. These particles were  
307 excluded from the final results. After excluding these very small particles, independent analyses  
308 of the 24 h sample performed by two different experimentalists differed in the average number  
309 and size of particles by only 7% and 2% respectively.

### 311 **3. Results**

#### 312 *3.1 Overview of the time course samples*

313 **Figure 2a** shows STXM maps of the Fe-containing particles in one cell from each time  
314 course point for the batch B samples. Early in the time course (10 m, 30 m), cells contained no or

1  
2  
3  
4  
5 315 just a few particles. The average Fe L<sub>3</sub> spectrum of all the particles within each cell in **Fig. 2a** are  
6  
7 316 plotted in **Fig. 2b**. Over the time course there is a general increase in the intensity of the Fe L<sub>3</sub>  
8  
9 317 signal, and some shape changes, which are discussed in a later section. A detailed description of  
10  
11 318 the particle size and number per cell at each time point in the batch B time course, as measured  
12  
13 319 by TEM is presented in section 3.2. In terms of particle numbers, there were no significant  
14  
15 320 differences between the samples taken at 10 m and 30 m after the start of the experiment,  
16  
17 321 followed by an increase in the number of particles per cell in subsequent time points. Cells from  
18  
19 322 the 1 h and 2 h sample exhibited only a few particles. A transition occurred in cells of the 4 h and  
20  
21 323 5.7 h samples, in which many more particles were present and chains started to appear. Cells in  
22  
23 324 samples taken at later times contained relatively large magnetite particles assembled in chains of  
24  
25 325 varying lengths. The average number of particles per cell and extent of chain formation at 48 h  
26  
27 326 were indistinguishable from stationary phase cells grown in Fe-rich media.

29  
30 327 **Supplemental figure S-1** shows STXM images of cells from **batch A** at each time point. In  
31  
32 328 the batch A experiments, particles appeared after 2 h in some cells. XAS spectra at the Fe L<sub>3</sub>  
33  
34 329 edge of particles from these experiments are presented in **Supplemental Fig. S-1g**. A systematic  
35  
36 330 increase in the X-ray absorption at ~710 eV of individual particles with time was observed. The  
37  
38 331 images and STXM-XAS results showed that a mixture of large and small particles was present in  
39  
40 332 cells from the 4 h sample. Only a few isolated particles were observed in the <2 h samples. By  
41  
42 333 48 h, STXM images of the cells examined were indistinguishable from STXM images of  
43  
44 334 stationary phase AMB-1 cells cultured in Fe-rich medium, both in terms of imaging (**Fig. S-1f**),  
45  
46 335 and Fe L<sub>3</sub> spectra (**Fig. S-1g**). On a qualitative basis, the trends seen in batch A and B are  
47  
48 336 similar.

### 52 338 *3.2 Statistics of particle size and number of particles per cell*

54 339 A stacked bar chart of the size distribution of particles per cell at each time point, as  
55  
56 340 determined by TEM, is shown in **Figure 3a**. The change over the time course in numbers within  
57  
58 341 each of 4 particle size ranges is presented on a log(time) plot in **Fig. 3b**. The numerical data is

1  
2  
3  
4  
5 342 presented in **Supplemental Table S-2** while **Fig. S-2** shows histograms of the size distribution at  
6  
7 343 each time point. Fig. 3b indicates there is a 30 m lag phase followed by growth of particles. This  
8  
9 344 is consistent with recent results on AMB-1 reported by Amor *et al.* (2018, 2019) in which they  
10  
11 345 find evidence for a similar lag phase, which they suggest correlates with the build-up of a pool of  
12  
13 346 intracellular iron, distinct from the magnetosomes. The average number of particles per cell was  
14  
15 347 about 13 after 2 h. Many of these particles were very small, probably below the spatial resolution  
16  
17 348 of STXM. Particle counts per cell for AMB-1 cells grown in an Fe-rich medium reported in the  
18  
19 349 literature range from 11 (Wang *et al.* 2013) to 20 (Tanaka *et al.* 2008).  
20

### 21 350 22 23 351 *3.3 Reference STXM – XAS/XMCD of mature AMB-1 magnetosomes*

24  
25 352 **Figure 4** presents a STXM image of a AMB-1 cell taken from stationary phase culture  
26  
27 353 grown in Fe-rich media, along with magnet maps, and the XAS and XMCD spectra of the  
28  
29 354 magnetosomes. The sample was tilted at 30° relative to the X-ray propagation direction and CR  
30  
31 355 was used. **Figure 4a** is the average of 36 OD images from 704 to 717 eV while **Fig. 4b** is a color  
32  
33 356 coded composite of component maps derived by fitting the Fe L<sub>3</sub> stack to the spectra presented in  
34  
35 357 **Fig. 4c**. The fitting identifies the magnetosomes with a parallel (red) and those with an  
36  
37 358 antiparallel (blue) alignment of their magnetic moment with respect to the circular polarization  
38  
39 359 vector of the photon (see **Fig. 1**). In **Fig. 4c** the dots are the average spectra of all the  
40  
41 360 magnetosomes with parallel (red) or anti-parallel (blue) magnetic alignment, while the solid lines  
42  
43 361 are spectra reported for synthetic magnetite (Goering *et al.* 2007) with their intensity scale  
44  
45 362 adjusted to match the OD of the AMB-1 magnetosome spectra. Although there is an offset, the  
46  
47 363 min-max magnitude of the XMCD signal in the AMB-1 magnetosomes is the same as that in  
48  
49 364 magnetically-saturated magnetite, indicating the magnetization of the magnetosomes is fully  
50  
51 365 saturated and the magnetic moment is oriented in the plane of the sample. A similar approach  
52  
53 366 was used to demonstrate that the magnetism of magnetosome in cells of *Magnetovibrio*  
54  
55 367 *blakemorei* strain MV1 is saturated (Kalirai *et al.* 2016). We note that normally CR and CL  
56  
57 368 spectra are normalized to the edge jump and presented as an asymmetry ratio. However, there  
58  
59  
60  
61  
62  
63  
64  
65

1  
2  
3  
4  
5 369 was not sufficient beam time to allow measurement of full Fe L<sub>23</sub> spectra for this type of  
6  
7 370 normalization.

8  
9 371 **Figure S-3** presents results from XAS-XMCD studies of two AMB-1 cells from the 48 h  
10  
11 372 time point in batch B, measured using CR with the sample tilted 30° relative to the X-ray beam.  
12  
13 373 In this case, in contrast to Fig. 4, the magnetic polarity of each magnetosome in an individual cell  
14  
15 374 is the same, but the magnetic moment of the chains in the left cell are pointing opposite to that in  
16  
17 375 the right cell, as shown by the color coded composite of signals from an XMCD stack map (**Fig**  
18  
19 376 **S-3a**). Full Fe L<sub>3</sub> stacks of the left cell were recorded using both CR and CL polarization, in  
20  
21 377 order to obtain the XAS and XMCD signals. **Fig. S-3b** compares the spectra of magnetosome  
22  
23 378 particles from the 48 h sample recorded with both circular polarizations, in comparison to the  
24  
25 379 data from **Fig. 4** and that of magnetite (Goering *et al.* 2007). The spectrum of the cytoplasm (also  
26  
27 380 plotted in **Fig. S-3b**) does not have any Fe L<sub>3</sub> signal. The CR stack was fit to the parallel and  
28  
29 381 anti-parallel reference spectra to generate component maps, which are presented as a color-coded  
30  
31 382 composite in **Fig. S-3c**. Within each color the signal for that component has been rescaled to the  
32  
33 383 full 0-255 scale. At the particles the parallel signal is strong while the anti-parallel signal is  
34  
35 384 weak, possibly just noise. The XMCD signal (**Fig. S-3b**) is strong, similar in intensity to that of  
36  
37 385 an AMB-1 cell taken from stationary phase culture grown in Fe-rich media (**Fig. 4**), and to that  
38  
39 386 of XMCD of magnetically saturated magnetite (Goering *et al.* 2007), scaled \*0.5 to account for  
40  
41 387 the experimental geometry (tilt angle of 30°).  
42  
43  
44 388

#### 45 389 *3.4 Time-dependent STXM-XAS Study of the Biomineralization Process*

46 390 Typically, 2 or 3 cells at each time point of the batch B time course were measured in detail.  
47  
48 391 In each case, there were only a few scattered individual particles present in cells up to 1 h.  
49  
50 392 Disordered chains and larger particles appear in cells from the 2 h sample. Well-developed  
51  
52 393 chains similar to those in cells from stationary phase culture grown in Fe-rich medium were  
53  
54 394 observed in cells from the 24 h and 48 h samples (see **Fig. 2a**). Cells from the 8 h time point of  
55  
56 395 batch A, and the 5.7 h and 24 h time points of batch B were particularly interesting and are  
57  
58 396 highlighted in the next sections.  
59  
60  
61  
62  
63  
64  
65

1  
2  
3  
4  
5 397 A detailed analysis of a cell from the 8 h sample in batch A is presented in **Fig. 5. Figure 5a**  
6  
7 398 shows that this cell contained one chain with 6 particles (left chain, red), a second chain in the  
8  
9 399 middle with 3 small particles (middle chain, cyan) which is interpreted as a “growing” chain, and  
10  
11 400 a third chain at the right with 3 very small particles which are interpreted as particles in the early  
12  
13 401 stages of growth (precursor, green). In addition, there is a single large magnetosome (blue).  
14  
15 402 **Figure 5b** compares the background subtracted Fe L<sub>3</sub> spectra of the large magnetosome, the left  
16  
17 403 chain, the middle (“growing”) chain and the chain of precursor particles from this cell, on an  
18  
19 404 absolute OD scale. **Fig. 5c** plots the same spectra on a constant intensity format, with  
20  
21 405 comparisons to reference spectra of FeCl<sub>3</sub> (Nagasaka, *et al.* 2013) and parallel and antiparallel  
22  
23 406 circular dichroic spectra of synthetic magnetite (Goering *et al.* 2007). The spectrum of the large  
24  
25 407 magnetosome is similar to that of magnetite with antiparallel magnetic moment orientation  
26  
27 408 relative to the CR light. The spectrum of the left chain is similar to that of magnetite with parallel  
28  
29 409 magnetic moment orientation relative to the CR light. In the spectrum of the particles in the  
30  
31 410 middle chain (cyan) the signal at 708.4 eV is significantly more intense than that of magnetite.  
32  
33 411 This is consistent with  $\alpha$ -hematite (Zhu *et al.* 2015). **Supplemental figure S-4** plots the Fe L<sub>3</sub>  
34  
35 412 spectra of several of the particles from early time course samples in comparison with the spectra  
36  
37 413 of  $\alpha$ -hematite (Zhu *et al.* 2015), ferrihydrite (Joshi *et al.* 2018), FeCl<sub>3</sub> (Nagasaka, *et al.* 2013)  
38  
39 414 and Fe(III) phosphate (Miot *et al.* 2009). While the differences are subtle, in the spectrum of the  
40  
41 415 particles of the 5h 40 m sample, the position and, especially, the intensity of the 708.4 eV signal  
42  
43 416 relative to the main peak at 709.8 eV is close to that of  $\alpha$ -hematite. However the spectrum of the  
44  
45 417 particles in the precursor chain of the 8 h sample is more similar to the Fe L<sub>3</sub> spectra of  
46  
47 418 ferrihydrite (Joshi *et al.* 2018) or FeCl<sub>3</sub> (Nagasaka, *et al.* 2013). The spectrum of the particles in  
48  
49 419 the “growing” chain is intermediate between the two, although closer to the spectrum of  
50  
51 420 magnetite.  
52  
53

54 421 To further focus on results from specific time course points, the STXM-XMCD results from  
55  
56 422 cells taken at the 5.7 h (5 h 40 m) and 24 h time points are discussed below. In addition, results  
57  
58 423 and discussion of the 4 h sample from batch B is given in the Supplemental Information. **Figure**  
59  
60  
61  
62  
63  
64  
65



1  
2  
3  
4  
5 424 **6** presents results from the 5.7 h sample (batch B) measured with the sample tilted at both  $0^\circ$  and  
6  
7 425  $30^\circ$  relative to the X-ray beam. In this case the cell examined was drop cast directly from the 5.7  
8  
9 426 h solution onto a C-flat grid, without washing. Despite that, the cell was very clean, without  
10  
11 427 adhering salts from the culture. **Fig. 6a** and **6b** present TEM images of the same cell, measured  
12  
13 428 after the STXM measurements. There are clear signs of carbon deposition in the rectangle  
14  
15 429 irradiated during the measurement (**Fig. 6a**). **Figure 6c** shows the sum of all images in an Fe  $L_3$   
16  
17 430 stack map, measured with the sample normal to the beam (tilt =  $0^\circ$ ). **Figure 6d** represents an  
18  
19 431 XMCD map at 708.2 eV measured at tilt =  $0^\circ$  showing that a number of the particles exhibit  
20  
21 432 out-of-plane magnetization. **Figure 6e** shows an XMCD map of the same set of particles,  
22  
23 433 measured at tilt =  $30^\circ$ . The XMCD signal intensity has significantly increased and all but the two  
24  
25 434 particles at the ends of the disorganized chain have the same magnetic moment direction, while  
26  
27 435 the magnetic moment of the particles at the end is in the opposite direction. The magnitude of the  
28  
29 436 XMCD signal of the leftmost particle is of opposite sign and twice as strong at  $0^\circ$  (-0.08) than at  
30  
31 437  $30^\circ$  tilt (+0.04). **Figure 6f** presents XAS measured with CR and CL polarization and the resulting  
32  
33 438 XMCD spectrum, averaged over all the particles in **Fig. 6e** which have a negative XMCD signal  
34  
35 439 (dark). A clear XMCD signal was obtained for this cell and the positioning of the particles was  
36  
37 440 such that chain formation appears to be occurring (**Fig. 6e**).

38  
39  
40 441 **Figure 7** plots the Fe  $L_3$  spectra of five different iron-containing regions of an AMB-1 cell  
41  
42 442 from the 24 h time point (batch B). Spectral variability in the Fe  $L_3$  stack was assessed by careful  
43  
44 443 examination of the Fe  $L_3$  spectra of the different morphologies. Five distinct Fe  $L_3$  spectra were  
45  
46 444 detected, which when used to fit the stack, resulted in a high quality fit with very small residuals  
47  
48 445 and clear, spatially localized component maps. A multivariate statistical analysis using the  
49  
50 446 PCA\_GUI code (Lerotic *et al.*, 2005) supported the existence of 6 or 7 independent components,  
51  
52 447 consistent with the analysis presented here. These spectra were used to derive the results  
53  
54 448 presented in **Fig. 8**, which includes component maps from the 5-component fit to the Fe  $L_3$  stack,  
55  
56 449 and a color coded composite map for cells of the 24 h sample (glutaraldehyde fixed). **Fig. 8a**  
57  
58 450 shows an OD-converted image of the full cell. **Fig. 8b** shows the average of all images in a

1  
2  
3  
4  
5 451 60-energy Fe L<sub>3</sub> stack measured on the right part of the cell, which has well-developed  
6  
7 452 magnetosome chains. The component maps, i.e., maps of the areas with spectra like one of the 5  
8  
9 453 reference spectra, are displayed in **Fig. 8c-g**. A color coded composite of the parallel XMCD  
10  
11 454 (red), cytoplasm (green) and antiparallel XMCD (blue) maps is presented in **Fig. 8h**. A notable  
12  
13 455 feature of this cell is a well-defined ‘ring’ or rim around the central, expanded part of the cell.  
14  
15 456 While the spectrum of the rim has a large non-Fe component, it also has a broad Fe L<sub>3</sub> signal  
16  
17 457 which is at higher energy than the Fe signal of the weak but statistically significant Fe L<sub>3</sub> signal  
18  
19 458 in the cytoplasm of the cell. Finally, one of the particles has a strong Fe(III) signal, different  
20  
21 459 from the small particles in the 5.7 h and 8 h cells which show enhanced 708.4 eV signal. That  
22  
23 460 Fe(III) particle did not exhibit any XMCD (compare **Fig. 8d** and **Fig. 8e, 8f**).  
24  
25 461

27 462 **Fig. 9** presents the circular dichroic dependent Fe L<sub>3</sub> XAS spectra and the derived XMCD  
28  
29 463 signal from the 10 magnetosomes in the 24 h cell (**Fig. 8e**). The intensity scale is that for the  
30  
31 464 optical density of the AMB-1 24 h cell data. **Fig. 9** also presents the parallel and antiparallel  
32  
33 465 spectra of magnetite reported by Goering *et al.* 2007, scaled to match the magnitude of the signal  
34  
35 466 from the AMB-1 cell. After correcting by a factor of 2 for the projection of the 30° tilted sample  
36  
37 467 onto the spin vector of the X-rays, the magnitudes of the XMCD signal of pure magnetite and  
38  
39 468 that of the magnetosomes are very similar. This indicates that, after 24 h of the time course, the  
40  
41 469 particles are magnetite and their magnetization is fully saturated.  
42  
43

44 470 **Supplemental Figure S-6** compares color-coded composites of the Fe-rich components  
45  
46 471 obtained from two different models for mapping the chemical components of the 24 h time point  
47  
48 472 sample from batch B from the Fe L<sub>3</sub> stack. **Fig. S-6a** was obtained from the stack measured with  
49  
50 473 CL using only 4 components (spectra of regions with XMCD+, XMCD-, cytoplasm and Fe(III),  
51  
52 474 without an explicit ‘rim’ signal) while **Fig. S-6b** was obtained from the stack measured with CR  
53  
54 475 using the 5 components displayed in **Fig. 7**. If a specific spectrum of the ‘rim’ is not included  
55  
56 476 then the area corresponding to the ‘rim’ is fit with the nominal CL component. However, if the  
57  
58 477 ‘rim’ spectrum is included in the fit then the rim signal fits to both the rim and regions in the  
59  
60  
61  
62  
63  
64  
65

1  
2  
3  
4  
5 478 vicinity of the magnetosomes. The model including an explicit rim spectrum is better.

6  
7 479 **Supplemental Figure S-7a-c** are images of the XMCD stack for the 24 h sample. **Figure S-7d**  
8  
9 480 displays the XMCD spectra of the magnetosomes while **Fig. S-7e** presents the XAS spectrum of  
10  
11 481 the rim. The XMCD spectrum of the 'rim', plotted in **Fig. S-7d**, showing there is no detectable  
12  
13 482 XMCD in the 'rim' region.

#### 14 15 483 16 17 484 18 19 485 **4. Discussion**

##### 20 486 *4.1 What we have learnt?*

21  
22  
23 487 Our results clearly show that small numbers of iron oxide particles were generated in cells of  
24  
25 488 *M. magneticum* strain AMB-1 grown without a major source of iron, relatively early (<30 m)  
26  
27 489 after the major source of iron, Fe(III) citrate, was introduced. These particles were significantly  
28  
29 490 smaller than those in magnetosomes in cells of cultures incubated for longer periods. The spectra  
30  
31 491 of the particles in cells taken at 10 m, 30 m, 1 h, and 2 h showed a signal at 708.4 eV that is  
32  
33 492 stronger than that of magnetite, indicating contributions from an Fe(III)-rich precursor. The  
34  
35 493 samples on TEM grids or SiN<sub>x</sub> windows were stored under dry N<sub>2</sub> from the time of preparation  
36  
37 494 to studies at SOLEIL. It has also been shown that magnetosome magnetite crystals which are  
38  
39 495 surrounded by their lipid membrane oxidize very slowly even when exposed to air for many  
40  
41 496 months (Zhu *et al.* 2015). Thus we conclude that the additional oxidized character of the smaller  
42  
43 497 particles in the early time points is a characteristic of the biomineralization of magnetite in *M.*  
44  
45 498 *magneticum*, and thus those particles can be considered precursors to magnetite. XMCD maps  
46  
47 499 (CR and CL at 708.2 eV, the energy of strongest XMCD contrast) and/or Fe L<sub>3</sub> stacks were  
48  
49  
50 500 measured for 5 of the 9 samples.

51  
52 501 One concern in interpreting these results is the question of the degree to which particles  
53  
54 502 observed at early time points might have been magnetite magnetosomes in cells inherited from  
55  
56 503 the original inoculum (which was grown in Fe-rich medium) or possibly even iron oxide  
57  
58 504 particles grown in Fe-depleted medium due to the presence of the very low concentration of Fe  
59  
60 505 required for cell growth, possibly present in Bacto<sup>TM</sup> Soytone. The 10 m samples in both batch A

1  
2  
3  
4  
5 506 and B contained a few cells with one particle that was quite large (40-50 nm) suggesting that it  
6  
7 507 could be a residual magnetosome from the original pre-Fe-depletion culture, despite many cycles  
8  
9 508 of re-inoculating in Fe-depleted medium to dilute the original cells and reduce the number of  
10  
11 509 magnetosomes per cell by allowing the cells to divide a significant number of times. Due to this  
12  
13 510 ambiguity we have placed greater reliance on samples at later time points ( $\geq 1$  h) in developing  
14  
15 511 our interpretation of these results.

16  
17 512 In cells from the 4 h sample from batch B, 1 out of 5 particles showed an XMCD signal with  
18  
19 513 the sample at  $0^\circ$  tilt. (**Fig. S-5**). The 4 small particles in the same cell did not exhibit a  
20  
21 514 measurable XMCD signal. Magnetosome crystals in cells grown for many generations in Fe-rich  
22  
23 515 growth medium only exhibit XMCD if the cell is  $\sim$ horizontal and tilted at  $30^\circ$  to the beam  
24  
25 516 propagation direction (Lam *et al.* 2010). The observation of a strong out-of-plane magnetization  
26  
27 517 is evidence that the magnetic particle was recently biomineralized. In the absence of chain  
28  
29 518 formation and presumably magnetic dipolar interaction with adjacent magnetite particles, the  
30  
31 519 magnetic moment could point in any direction. If the particle-particle magnetic interaction  
32  
33 520 between pre-existing magnetosome(s) and a newly biomineralized magnetosome(s) is not strong  
34  
35 521 enough to align the magnetic vector of the new one, the magnetic orientation of the newly  
36  
37 522 forming magnetosome would be determined by external factors such as the local magnetic field  
38  
39 523 of the earth at the time of particle formation. Winklhofer *et al.* (2007) reported that the degree of  
40  
41 524 preferential alignment was 0.54:0.46 at a magnetic field of 0.26 G (about that of the earth in  
42  
43 525 Hamilton, ON where the time course samples were grown) and rose only to 0.58:0.42 at a field  
44  
45 526 of 0.50 G.

46  
47 527 It should be noted that the visual gap between magnetosomes with opposite magnetic  
48  
49 528 polarities (e.g. **Fig. 6e**) might not represent the real distance between these magnetosomes, since  
50  
51 529 2D projection images can mask the actual 3D distance information. In this regard, XMCD  
52  
53 530 tomography, which can map the magnetization strength and direction of individual particles in  
54  
55 531 3D, of a cell displaying both in-plane and out-of-plane magnetization might provide additional  
56  
57 532 insight into how MTB achieve the well organized and well correlated magnetism of adjacent  
58  
59 533 magnetosomes. Electron tomography was very useful in showing that lipid vesicles in which  
60  
61  
62  
63  
64  
65

1  
2  
3  
4 534 magnetosomes are formed bud from the exterior cell membrane (Komeli *et al.*2004). Cells from  
5  
6 535 the 5.7 h batch B contained numerous particles (>12 /cell on average), the crystals in some of  
7  
8 536 which exhibited XMCD at 0° with opposing moment orientations (**Fig. 6**). When the same  
9  
10 537 sample was measured at 30°, an XMCD signal was observed for the majority of the particles,  
11  
12 538 indicating a chain with a more organized magnetic structure was being formed. In cells from the  
13  
14 539 24 and 48 h samples, the XAS spectra measured at 30° and the magnitude of the derived XMCD  
15  
16 540 signal of the magnetosomes was similar to that of synthetic magnetite (Goering *et al.* 2007) (**Fig.**  
17 541 **S-3b**).

18  
19 542 Iron oxide particles were observed in cells from the 1 – 8 h time points which had a  
20  
21 543 measurably smaller diameter and weaker Fe L<sub>3</sub> signal than that of mature paticles found in  
22  
23 544 AMB-1 cells, and typically a stronger signal at 708.4 eV than is expected for magnetite. These  
24  
25 545 particles are interpreted as growing particles and thus their properties are providing direct  
26  
27 546 information about the biomineralization mechanism. The stronger 708.4 eV signal is evidence  
28  
29 547 for a higher Fe(III) character than that of magnetite. The comparison of the position and intensity  
30  
31 548 of the 708.4 eV signal relative to the main 709.8 eV peak with that in other Fe(III) compounds  
32 549 (**Fig. S-4**), suggests that  $\alpha$ -hematite (Zhu *et al.* 2015) is a possible intermediate in the  
33  
34 550 development of mature magnetosomes. We note that  $\alpha$ -hematite was also found in previous time  
35  
36 551 course studies by Baumgartner *et al.* (2013) and Firlar *et al.* (2016, 2019), although both of those  
37  
38 552 studies, along with that by Fdez-Gubieda *et al.* (2013), concluded that a phosphate-rich ferric  
39  
40 553 hydroxide phase was involved. We also find a precursor signal consistent with FeCl<sub>3</sub> and/or  
41  
42 554 ferrihydrite, in agreement with the main conclusions of Baumgartner *et al.* (2013) and  
43  
44 555 Fdez-Gubieda *et al.* (2013). A better understanding of the role of these two species in the  
45  
46 556 biomineralization pathway is now required. We note that the statistical quality of the Fe L<sub>3</sub>  
47  
48 557 spectra from the particles in the earlier time points is limited. In addition the spectra are averaged  
49  
50 558 over several particles, which may be at different stages of development and thus might have  
51  
52 559 different speciation. Finally, we did not have enough beam time to adequately sample times  
53  
54 560 below 1 hour and thus our results are silent in that early period, where Wen *et al.* (2019) find  
55  
56 561 evidence for  $\epsilon$ -Fe<sub>2</sub>O<sub>3</sub> from single particle electron diffraction.

56 562 A striking observation in this study is that small particles are formed at multiple places in the  
57  
58 563 cell, not necessarily in chains, and with seemingly no detectable ferromagnetism, or with  
59  
60 564 randomly oriented magnetic moments. The observation of these putative precursor particles in  
61  
62  
63  
64  
65

1  
2  
3  
4 565 different cell locations and at different times time course points suggests that magnetosomes are  
5  
6 566 not biomineralized simultaneously. Regarding the appearance of precursors at multiple sites  
7  
8 567 within the cell, Scheffel *et al.* (2006) have shown that magnetite biomineralization is initiated at  
9  
10 568 multiple discrete sites throughout the length of *Magnetospirillum* cells. Thus mature  
11  
12 569 magnetosomes and magnetosome precursors can coexist in the same cell since some may grow  
13  
14 570 faster than others. The acidic protein MamJ was shown to be responsible for anchoring the  
15  
16 571 magnetosome to a filamentous structure now recognized as the protein MamK (Arakaki *et al.*  
17  
18 572 2008). As for the lack of ferromagnetism observed in these precursors, this could be because  
19  
20 573 these small particles are not (yet) magnetite and thus not magnetic at room temperature.  
21  
22 574 Alternatively they could be smaller than the ~30 nm super-paramagnetic limit in magnetite  
23  
24 575 (Dunlop 1973), and thus subject to thermally induced re-orientation of their magnetic moment. A  
25  
26 576 third explanation could be that the early particles are Fe-rich polyphosphates formed in the  
27  
28 577 cytoplasm, as was found in some other bacterial systems (Miot *et al.* 2009). STXM  
29  
30 578 measurements at the P 2p or P 1s edge could be used to investigate this last possibility.

31  
32 579 In the intermediate time points (4 – 8 h) chain formation is increasingly seen, and a larger  
33  
34 580 fraction of the particles are located in chains with an in-plane magnetic moment (e.g. the 5.7 h  
35  
36 581 batch B sample, **Fig. 6**, and the 8 h batch A sample, **Fig. 5**). It is only in the 24 h and 48 h  
37  
38 582 samples that the size, spectroscopy, magnetic moment magnitude and orientation match that of  
39  
40 583 magnetosome chains in mature AMB-1 cells grown in Fe-rich culture.

41 584 From a microbiological point of view, this study shows that *M. magneticum* strain AMB-1  
42  
43 585 will grow for extended periods of time when several nutrient sources usually added to the growth  
44  
45 586 medium are omitted or added in significantly lower concentration – in this case, yeast extract,  
46  
47 587 Bacto™ Soytone, mineral solution in addition to Fe(III) citrate, the major Fe source of the  
48  
49 588 normal growth medium. Increasing the O<sub>2</sub> concentration does not prevent growth either, showing  
50  
51 589 that *M. magneticum* can adapt to a relatively wide range of conditions, from microaerobic to  
52  
53 590 fully oxic conditions. When cultured at high concentrations of O<sub>2</sub> and low concentrations of Fe  
54  
55 591 for extended periods of time, the cells biomineralize only a few crystals and grow as vigorously  
56  
57 592 as in normal media. These findings raise important questions regarding the magneto-aerotaxis  
58  
59 593 model for the function of magnetosomes in magnetotactic bacteria, at least for *M. magneticum*. If

1  
2  
3  
4  
5 594 the cells grow in presence of high concentrations of O<sub>2</sub> expending energy to produce  
6  
7 595 magnetosomes no longer seems advantageous if their only role is to help the cells locate the OAI  
8  
9 596 more efficiently. Finally, as seen during this and other time course experiments, cells start  
10  
11 597 biomineralizing new crystals quite quickly once placed under low O<sub>2</sub> and relatively high Fe  
12  
13 598 concentrations. This shows that the machinery used to perform biomineralization is conserved  
14  
15 599 during periods of Fe starvation and that it is quickly reactivated when the environmental  
16  
17 600 conditions are suitable.

#### 19 601 20 21 602 *4.2 Suggestions for future studies*

23 603 While these results contribute to our understanding of magnetosome biomineralization, they  
24  
25 604 are still ambiguous with regard to the identity of the Fe(III)-rich precursor species. Many studies  
26  
27 605 have shown that it is possible to use XAS and XMCD to differentiate among the candidate  
28  
29 606 species ( $\alpha$ -hematite, Fe phosphates, ferrihydrite). However better statistics than we were able to  
30  
31 607 achieve in this study are required. In part this is a function of limited experimental time at the  
32  
33 608 synchrotron STXM, and in part a consequence of limited spatial resolution. The former issue can  
34  
35 609 be addressed by focusing on just a few representative cells in the 1-6 h time course points where  
36  
37 610 the evolution of the chemistry and organization is occurring. More precise spectra could then be  
38  
39 611 fit to a linear combination of the 2 contributions and used to extract the ratio of the precursor and  
40  
41 612 magnetite components as a function of time. Higher spatial resolution can be achieved by using  
42  
43 613 the emerging method of soft X-ray ptychography (Thibault *et al.* 2014, Hitchcock 2015) which  
44  
45 614 has already been applied to MV-1 MTB (Zhu *et al.* 2016). In addition to XAS and XMCD in 2D  
46  
47 615 projection, it would be beneficial to perform XMCD tomography in order to locate the spatial  
48  
49 616 orientation of the magnetic moment of particles in cells like the 5.7 h sample (**Fig. 6**).

#### 51 617 52 53 54 618 **5. Summary**

56 619 This work has presented results of a time course study of an intracellular biomineralization  
57  
58 620 process elaborating the formation of mature magnetite magnetosomes in cells of the  
59  
60  
61  
62  
63  
64  
65

1  
2  
3  
4  
5  
6  
7  
8  
9  
10  
11  
12  
13  
14  
15  
16  
17  
18  
19  
20  
21  
22  
23  
24  
25  
26  
27  
28  
29  
30  
31  
32  
33  
34  
35  
36  
37  
38  
39  
40  
41  
42  
43  
44  
45  
46  
47  
48  
49  
50  
51  
52  
53  
54  
55  
56  
57  
58  
59  
60  
61  
62  
63  
64  
65

621 magnetotactic bacterium *M. magneticum* strain AMB-1. Our results indicate that the  
622 initially-produced particles are Fe(III)-rich. Later, some of the Fe(III) is reduced to form  
623 magnetite. The particles in the growth phase are primarily disorganized but start forming  
624 organized chains at about 4 h of growth and reach a mature stage between 24 to 48 h, with  
625 number per cell and size of the magnetosomes similar to that observed in cells at saturation phase  
626 grown in Fe-rich culture. Our results are consistent with most previous studies which report the  
627 presence of some type of excess Fe(III) during early growth. However, few of these studies  
628 resulted in the identification of a specific Fe(III)-rich species. Our Fe L<sub>3</sub> XAS results suggest  
629  $\alpha$ -hematite is a precursor to magnetite in AMB-1, but do not exclude other possible precursors  
630 such as ferrihydrite. Future studies will reveal whether these two species contribute to the same  
631 or to distinct pathways towards magnetite. In addition, this work provides additional insight into  
632 the magnetite biomineralization mechanism through detailed Fe L<sub>3</sub> XAS and XMCD spectra of  
633 precursors and immature magnetosomes.

634  
635 **Acknowledgements:** This work was supported by NSERC (Canada) (Hitchcock) and by the U.S.  
636 National Science Foundation grant EAR-1423939 (Bazylinski). The measurements were carried  
637 out at the STXM on the Hermes beamline at Synchrotron SOLEIL. We thank Marcia Reid for  
638 excellent assistance with TEM viewing and preparation of the gluteraldehyde fixed samples.

639  
640 **References**

641 Arakaki, A., Nakazawa, H., Nemoto, M., Mori, T., Matsunaga, T. (2008) Formation of magnetite by  
642 bacteria and its application, *J. R. Soc., Interface*, 5, 977–999.

643 Amor, M., Busigny, V., Louvat, P., Tharaud, M., Gélabert, A., Cartigny, P., Carlut, J., Isambert, A.,  
644 Durand-Dubief, M.I., Ona-Nguema, G., Alphantery, E., Chebbid, I., Guyot, F. (2018) Iron uptake and  
645 mag-netite biomineralization in the magnetotactic bacterium *Magnetospirillum magneticum* strain AMB-1:  
646 an iron iso-tope study. *Geochem. Cosmochem. Acta* 232, 225–243

647 Amor, M., Tharaud, M., Gelabert, Komeili, A., (2019) Single-cell determination of iron content in  
648 magnetotactic bacteria: implications for the iron biogeochemical cycle, *Environmental Microbiology*,  
649 XX, YYY-YYY. doi: 10.1111/1462-2920.14708



1  
2  
3  
4 650 Bazylinski, D.A. (1999) Synthesis of the bacterial magnetosome: the making of a magnetic personality  
5  
6 651 *International Microbiology*, 2, 71-80  
7  
8 652 Bazylinski, D.A., Dean, A.J., Schüler, D. Phillips, E.J.P., Lovley, D.R. (2000) N<sub>2</sub>-dependent growth and  
9  
10 653 nitrogenase activity in the metal-metabolizing bacteria, *geobacter* and *magnetospirillum* species.  
11  
12 654 *Environmental Microbiology*, 2, 266–273.  
13  
14 655 Bazylinski, D.A., Frankel, R.B., Heywood, B.R., Mann, S., King, J.W., Donaghay, P.L., Hanson, A.K.,  
15  
16 656 (1995) Controlled biomineralization of magnetite (Fe<sub>3</sub>O<sub>4</sub>) and greigite (Fe<sub>3</sub>S<sub>4</sub>) in a magnetotactic  
17  
18 657 bacterium. *Applied and Environmental Microbiology* 61, 3232–3239.  
19  
20 658 Baumgartner, J., Morin, G., Menguy, N. Gonzalez, T.P., Widdrat, M., Cosmidis, J., Faivre, D. (2013)  
21  
22 659 Magnetotactic bacteria form magnetite from a phosphate-rich ferric hydroxide via nanometric ferric  
23  
24 660 (oxyhydr)oxide intermediates, *Proc. Nat. Acad. Sci.* 110, 14883–14888.  
25  
26 661 Belkhou, R., Stanescu, S., Swaraj, S., Besson, A., Ledoux, M., Hajlaoui, M. Dalle, D. (2015) HERMES: a  
27  
28 662 soft X-ray beamline dedicated to X-ray microscopy, *J. Synchrotron Radiation*, 22(4): 968-979.  
29  
30 663 Cazares. L.H., Van Tongeren, S.A., Costantino J., Kenny, T., Garza, N.L., Donnelly, G., Lane, D., Panchal,  
31  
32 664 R.G., Bavari, S. (2015) Heat fixation inactivates viral and bacterial pathogens and is compatible with  
33  
34 665 downstream MALDI mass spectrometry tissue imaging, *B.M.C. Microbiology* 15: 101 (1-11).  
35  
36 666 Chen, A.P., Berounsky, V.M., Chan, M.K., Blackford, M.G., Cady, C., Moskowitz, B.M., Kraal, P.,  
37  
38 667 Lima, E.A., Kopp, R.E., Lumpkin, G.R., Weiss, B.P., Hesse, P., Vella, N.G.F. (2014) Magnetic  
39  
40 668 properties of uncultivated magnetotactic bacteria and their contribution to a stratified estuary iron cycle.  
41  
42 669 *Nature Communications*, 5, 4797.  
43  
44 670 Chen T., Wang, Z., Wu, X. Gao, X. Li, L., Zhan, Q.(2015) Magnetic properties of tidal flat sediments on  
45  
46 671 the Yangtze coast, China: Early diagenetic alteration and implications, *The Holocene* 25, 832-843.  
47  
48 672 Chao, Y, Zhang, T. (2011) Optimization of fixation methods for observation of bacterial cell morphology  
49  
50 673 and surface ultrastructures by atomic force microscopy, *Appl. Microbiol. Biotechnology* 92, 381-392.  
51  
52 674 Cosmidis, J., Benzerara, K., Morin, G., Busigny, V., Lebeau, O., Othmane, G., Dublet, G., Noel, V.  
53  
54 675 (2014) Biomineralization of iron-phosphates in the water column of Lake Pavin (Massif Central, France),  
55  
56 676 *Geochimica et Cosmochimica Acta* 126, 78-96.  
57  
58 677 Dunlop, D.J. (1973) J. Superparamagnetic and Single-Domain Threshold Sizes in Magnetite, *Geophysical*  
59  
60 678 *Research* 78, 1780-1793  
61  
62  
63  
64  
65

1  
2  
3  
4 679 Faivre, D., Schuler, D. (2008). Magnetotactic Bacteria and Magnetosomes, Chem. Rev. 108,  
5  
6 680 4875-4898.  
7  
8 681 Faivre, D., Böttger, L.H., Matzanke, B.F., Schüler, D. (2007) Intracellular Magnetite Biomineralization in  
9  
10 682 Bacteria Proceeds by a Distinct Pathway Involving Membrane- Bound Ferritin and an Iron(II) Species,  
11  
12 683 Angew. Chem., Int. Ed. Engl. 46, 8495-8499.  
13  
14 684 Fdez-Gubieda, M.L., Muela, A., Alonso, J., García-Prieto, A., Olivi, L., Fernández-Pacheco, R., &  
15  
16 685 Barandiarán, J. M. (2013) Magnetite biomineralization in *Magnetospirillum gryphiswaldense*:  
17  
18 686 time-resolved magnetic and structural studies. ACS nano, 7(4), 3297-3305.  
19  
20 687 Firlar, E., Perez-Gonzalez, T., Olszewska, A., Faivre, D., Prozorov, T., (2016) Following iron speciation  
21  
22 688 in the early stages of magnetite magnetosome biomineralization, J. Mater. Res. 31, 547-555  
23  
24 689 Firlar, E., Ouy, M., Bogdanowicz, A., Covnot, L., Song, B., Nadkarni, Y., Shahbazian-Yassar, R.,  
25  
26 690 Shokuhfar T. (2019) Investigation of the magnetosome biomineralization in magnetotactic bacteria using  
27  
28 691 graphene liquid cell – transmission electron microscopy, Nanoscale 11, 698-705.  
29  
30 692 Frankel, R. B., Papaefthymiou, G.C., Blakemore, R.P., O'Brien W. (1983) Fe<sub>3</sub>O<sub>4</sub> precipitation in  
31  
32 693 magnetotactic bacteria, Biochim. Biophys. Acta 763, 147-159.  
33  
34 694 Goering E., Lafkioti M., Gold S., Schuetz G.. (2007) Absorption Spectroscopy and XMCD at the Verwey  
35  
36 695 Transition of Fe<sub>3</sub>O<sub>4</sub>, J. Magnetism and Magnetic Materials 310, e249–e251.  
37  
38 696 HeyenU., Schüler D. (2003) Growth and magnetosome formation by microaerophilic *Magnetospirillum*  
39  
40 697 strains in an oxygen-controlled fermentor, Appl. Microbiol. Biotechnol. 61, 536–544.  
41  
42 698 Hitchcock, A.P. (2012) Soft X-ray Imaging and Spectromicroscopy, Chapter 22, Volume II of the  
43  
44 699 *Handbook on Nanoscopy*, eds. Gustaaf Van Tendeloo, Dirk Van Dyck and Stephen J. Pennycook (Wiley)  
45  
46 700 745-791.  
47  
48 701 Hitchcock, A.P., (2015) Soft X-ray spectromicroscopy and ptychography, J. Electron Spectroscopy and  
49  
50 702 Related Phenomena 200, 49-63.  
51  
52 703 Jogler, C. Schüler, D. (2007) in *Genetic Analysis of Magnetosome Biomineralization BT –*  
53  
54 704 *Magnetoreception and Magnetosomes in Bacteria*, ed. D. Schüler, D., Springer Berlin Heidelberg, Berlin,  
55  
56 705 Heidelberg, 133–161.  
57  
58 706 Joshi, N., Filip, J. Coker, V.S., Sadhukhan, J., Safarik, I., Bagshaw,H., Lloyd, J.R. (2018) Microbial  
59  
60 707 Reduction of Natural Fe(III) Minerals; Toward the Sustainable Production of Functional Magnetic  
61  
62 708 Nanoparticles, Frontiers in Env. Sci. 6, 127.  
63  
64  
65

1  
2  
3  
4 709 Kalirai, S.S., Lam, K.P., Bazylinski, D.A., Lins, U., A.P. Hitchcock, A.P. (2012) Examining the  
5  
6 710 chemistry and magnetism of magnetotactic bacterium *Candidatus Magnetovibrio blakemorei* strain MV-1  
7  
8 711 using scanning transmission X-ray microscopy, *Chemical Geology* 300-301, 14-23.  
9  
10 712 Komeili A, Vali H, Beveridge TJ, Newman DK (2004) Magnetosome vesicles are present before  
11  
12 713 magnetite formation, and MamA is required for their activation *Proc Natl Acad Sci USA* 101,  
13  
14 714 3839–3844.  
15  
16 715 Lam, K.P., Hitchcock, A.P. , Obst, M., Lawrence, J.R., Swerhone, G..D.W., Leppard, G..G.,  
17  
18 716 Tyliszczak, T. , Karunakaran, C., Wang, J., Kaznatcheev, K., Bazylinski, D., Lins, U. (2010) X-ray  
19  
20 717 magnetic circular dichroism of individual magnetosomes by Scanning Transmission X-ray Microscopy,  
21  
22 718 *Chemical Geology* 270, 110-116.  
23  
24 719 Lefèvre, C. T., & Bazylinski, D. A. (2013). Ecology, diversity, and evolution of magnetotactic bacteria.  
25  
26 720 *Microbiol. Mol. Biol. Rev.*, 77(3), 497-526.  
27  
28 721 Le Nagard, L. , Zhu, X.H. , Hitchcock, A.P., Bazylinski, D.A., Swaraj, S., Stanescu, S., Belkhou, R.  
29  
30 722 (2018a) How do Magnetotactic Bacteria Synthesize Magnetite? – a Soft X-ray Spectroscopy,  
31  
32 723 Spectromicroscopy and Magnetism Time Course Study, *Microscopy & Microanalysis* 24, 376-377.  
33  
34 724 Le Nagard, L., Morillo-López, V, Fradin, C. Bazylinski, D.A. (2018b), Growing Magnetotactic Bacteria of  
35  
36 725 the Genus *Magnetospirillum*: Strains MSR-1, AMB-1 and MS-1, *JOVE* 140, DOI: 10.3791/58536  
37  
38 726 Lerotic, M., Jacobsen, C., Gillow, J.B., Francis, A.J., Wirick, S., Vogt, S., Maser J. (2005) Cluster  
39  
40 727 analysis in soft X-ray spectromicroscopy: Finding the patterns in complex specimens, *J. El. Spec. Rel.*  
41  
42 728 *Phen.* 144, 1137-1143.  
43  
44 729 Li, J., Pan, Y.X. , Chen, G., Liu, Q., Tian, L.X., Lin , W. (2009) Magnetite magnetosome and fragmental  
45  
46 730 chain formation of *Magnetospirillum magneticum* AMB-1: Transmission electron microscopy and  
47  
48 731 magnetic observations, *Geophys. J. Int.* 177, 33-42.  
49  
50 732 Li, J., Benzerara, K., Bernard, S., Beyssac, O.(2013) The link between biomineralization and fossilization  
51  
52 733 of bacteria: Insights from field and experimental studies, *Chemical Geology* 359, 49-69.  
53  
54 734 Lin, W., Bazylinski, D.A., Xiao, T., Wu, L.-F., Pan, Y., (2014) Life with compass: diversity and  
55  
56 735 biogeography of magnetotactic bacteria, *Environmental Microbiology* 19, 2646-2658.  
57  
58 736 Lin, W., Paterson, G.A., Zhuc Q., Wang, Y., Kopylova, E., Lie, Y., Knight, R., Bazylinski, D.A., Zhuh, R.,  
59  
60 737 Kirschvink, J.L., Pan, Y. (2017) Origin of microbial biomineralization and magnetotaxis during the  
61  
62 738 Archean, *Proc Natl Acad Sci U S A.* 114, 2171-2176.  
63  
64  
65

1  
2  
3  
4 739 Marcano, L., García-Prieto, A., Muñoz, D., Barquín, L. F., Orue, I., Alonso, J., Muella, A.,  
5  
6 740 Fdez-Gubieda, M.L. (2017). Influence of the bacterial growth phase on the magnetic properties of  
7  
8 741 magnetosomes synthesized by *Magnetospirillum gryphiswaldense*. *Biochimica et Biophysica Acta*  
9 742 (BBA)-General Subjects, 1861(6), 1507-1514.  
10  
11 743 Miot, J., Benzerara, K., Morin, G., Kappler, A., Bernard, S., Obst, M., Férard, C., Skouri-Panet, F.,  
12  
13 744 Guigner, J.-M., Posth, N., Galvez, M., Brown Jr, G.E. Guyot, F. (2009) Iron biomineralization by  
14  
15 745 anaerobic neutrophilic iron-oxidizing bacteria, *Geochimica et Cosmochimica Acta* 73, 696–711.  
16  
17 746 Nagasaka M, Yuzawa, H., Horigome, T., Hitchcock. A.P., Kosugi, N. (2013) Electrochemical reaction of  
18  
19 747 aqueous iron sulfate solutions studied by Fe L-edge soft X-ray absorption spectroscopy. *J Phys Chem C*  
20 748 117(32): 16343–16348.  
21  
22  
23 749 Murat D., Falahati V., Bertinetti L., Csencsits R., Körnig A., Downing K., Faivre D., Komeili A. (2012)  
24  
25 750 The magnetosome membrane protein, MmsF, is a major regulator of magnetite biomineralization in  
26  
27 751 *Magnetospirillum magneticum* AMB-1, *Molecular Microbiology* 85, 684-699.  
28  
29 752 Rivas-Lamelo, S., Benzerara, K., Lefèvre, C., Monteil, C., Jézéquel, D., Menguy, N., Viollier, E., Guyot,  
30  
31 753 F., Férard, C., Poinso, M., Skouri-Panet, F., Trcera, N., Miot, J., Duprat, E. (2017) Magnetotactic  
32  
33 754 bacteria as a new model for P sequestration in the ferruginous Lake Pavin. *Geochemical Perspectives*  
34 755 *Letters*, 5, 35-41.  
35  
36 756 Scheffel, A., Gruska, M., Faivre, M., Linaroudis, A., Plitzko, J.M., Schüler, D. (2006) An acidic protein  
37  
38 757 aligns magnetosomes along a filamentous structure in magnetotactic bacteria. *Nature*, 440, 110-114.  
39  
40 758 Schulz-Vogt H.N., Pollehne F., Jürgens K., Arz H.W., Beier S., Bahlo R., Dellwig O., Henkel J.V.,  
41  
42 759 Herlemann D.P.R., Krüger S., Leipe T., Schott T. (2019) Effect of large magnetotactic bacteria with  
43  
44 760 polyphosphate inclusions on the phosphate profile of the suboxic zone in the Black Sea. *ISME J.* 13,  
45 761 1198-1208.  
46  
47 762 Staniland, S., Ward, B., Harrison, A., van der Laan, G., Telling, N. (2007) Rapid magnetosome formation  
48  
49 763 shown by real-time x-ray magnetic circular dichroism, *Proc. Nat. Acad. Sci.* 104, 19524-19528.  
50  
51 764 Swaraj, S., Belkhou, R., Stanescu, S., Rioult, M., Besson, A., Hitchcock, A.P. (2017) Performance of the  
52  
53 765 HERMES beamline at the carbon K-edge, *IOP Conference Series: J. Phys. Conf. Series* 849, 012046  
54  
55 766 Tanaka, M., Nakata, Y., Mori, T., Okamura, Y., Miyasaka, H., Takeyama, H., Matsunaga, T. (2008)  
56  
57 767 Development of a Cell Surface Display System in a Magnetotactic Bacterium, “*Magnetospirillum*  
58  
59 768 *magneticum*” AMB-1. *Applied and Environmental Microbiology* 74, 3342-3348.  
60  
61  
62  
63  
64  
65

1  
2  
3  
4 769 Thibault, P., Guizar-Sicairos, M., Menzel, A. (2014) Coherent imaging at the diffraction limit J.  
5  
6 770 Synchrotron Rad. 21, 1011–1018.  
7  
8 771 Wang, Y., Lin, W., Li, J., Pan, Y. (2013) Changes of cell growth and magnetosome biomineralization in  
9  
10 772 *Magnetospirillum magneticum* AMB-1 after ultraviolet-B irradiation, Frontiers in Microbiology,  
11  
12 773 Intracellular Biomineralization in Bacteria (eds. Lin, W., Benerara, K., Faivre, D. Pan, Y.)  
13  
14 774 Wen, T., Zhang, Y., Geng Y., Liu, J., Basit, A., Tian, J., Li, Y., Li, J., Ju, J., Jiang, W. (2019)  
15  
16 775 Epsilon-Fe<sub>2</sub>O<sub>3</sub> is a novel intermediate for magnetite biosynthesis in magnetotactic bacteria, Biomaterials  
17  
18 776 Research 23, 13 (1-7).  
19  
20  
21 777 Winklhofer M, Abracado LG, Davila AF, Keim CN, Lins de Barros HGP (2007) Magnetic optimization  
22  
23 778 in a multicellular magnetotactic organism. Biophys. J. 92: 661–670.  
24  
25 779 Wolin, E.A, Wolin, M.J., Wolfe, R.S. (1963) Formation of methane by bacterial extracts. J. Biological  
26  
27 780 Chemistry, 238, 2882–2886.  
28  
29 781 Zhu, X.H., Kalirai, S.S., Hitchcock, A.P. Bazylinski, D.A. (2015) What is the correct Fe L<sub>23</sub> X-ray  
30  
31 782 absorption spectrum of magnetite?, J. Electron Spectroscopy and Rel. Phenom. 199, 19-26.  
32  
33 783 Zhu, X. H., Hitchcock, A.P., Bazylinski, D.A., Denes, P., Joseph, J., Lins, U., Marchesini, S. , Shiu,  
34  
35 784 H.-W., Tyliczszak, T., Shapiro, D.A. (2016) Measuring spectroscopy and magnetism of extracted and  
36  
37 785 intracellular magnetosomes using soft X-ray ptychography, Proc. Nat. Acad. Sci 113, E8219- E8227.  
38  
39 786  
40  
41  
42  
43  
44  
45  
46  
47  
48  
49  
50  
51  
52  
53  
54  
55  
56  
57  
58  
59  
60  
61  
62  
63  
64  
65

1  
2  
3  
4  
5 **787 Figure Captions**

6  
7 **788 Figure 1** Schematic of XMCD as applied to magnetotactic bacteria. (a) 3D view for tilt = 0°,  
8  
9 **789** with the vector for circular right (CR) polarization along the X-ray propagation direction (black)  
10  
11 **790** and the sample with 3 possible in-plane magnetization vectors (red, blue - horizontal, green -  
12  
13 **791** vertical). (b) Top view for tilt = 0°. There is no XMCD signal since the dot product of the photon  
14  
15 **792** polarization and each of the sample magnetization vectors is 0. (c) 3D view for polar angle tilt of  
16  
17 **793** 30°. (d) Top view for tilt = 30°. There is a 50% XMCD signal with both parallel (red) and  
18  
19 **794** antiparallel (blue) alignment of an in-plane, horizontal sample magnetization. If the sample  
20  
21 **795** magnetization is vertical (green) no XMCD would be observed at any polar tilt angle.  
22

23  
24 **796**  
25  
26 **797 Figure 2** (a) Images of particles in individual cells from the 9 time course points of batch B. In  
27  
28 **798** each case the image is  $OD_{\text{peak}} - OD_{\text{pre}}$  where  $OD_{\text{peak}}$  is average of 8 images from 707.5 to 711.5  
29  
30 **799** eV, and  $OD_{\text{pre}}$  is average of 8 images from 702 to 706 eV. Scale bar is 200 nm in each case. (b)  
31  
32 **800** Fe L<sub>3</sub> spectra of particles extracted from stacks measured on the cells in Fig 2a. The zero of each  
33  
34 **801** spectrum is indicated on the vertical axis. The OD/cm scaling is the same for each spectrum. The  
35  
36 **802** arrow indicates the shoulder at 708.4 eV, which is more prominent in the spectra of particles at  
37  
38 **803** the 10 m, 30 m and 2 h time course.  
39

40  
41 **804**  
42  
43 **805 Figure 3** (a) Stacked bar chart of the numbers and distribution of sizes of the particles per cell  
44  
45 **806** derived from TEM images at each of the 9 time course points (batch B). The protocols used to  
46  
47 **807** achieve an accurate and unbiased distribution are discussed in the text. (b) evolution of numbers  
48  
49 **808** of particles within particle size ranges as a function of log(time). There is a 30 m lag phase  
50  
51 **809** followed by logarithmic growth of particles. Error bars not included for clarity. The  
52  
53 **810** corresponding numerical data, including standard deviation, are shown in Table S-2.  
54  
55

56 **811**  
57  
58  
59  
60  
61  
62  
63  
64  
65

1  
2  
3  
4  
5  
6  
7  
8  
9  
10  
11  
12  
13  
14  
15  
16  
17  
18  
19  
20  
21  
22  
23  
24  
25  
26  
27  
28  
29  
30  
31  
32  
33  
34  
35  
36  
37  
38  
39  
40  
41  
42  
43  
44  
45  
46  
47  
48  
49  
50  
51  
52  
53  
54  
55  
56  
57  
58  
59  
60  
61  
62  
63  
64  
65

**Figure 4** (a) Average of 36 optical density (OD) images from 704 to 717 eV of an AMB-1 cells from a high Fe content culture of AMB-1 grown over an extended time period. The polarization was circular right (CR) and the sample was tilted 30° relative to the X-ray beam. The numbers at the right side of the image are the OD limits of the grey scale. (b) Color coded composite of component maps derived from a fit of the Fe L<sub>3</sub> stack to spectra for parallel (red), antiparallel (blue) magnetite and the no-Fe signal of the non-magnetite cell contents (green). The arrows indicate the directions of the parallel and antiparallel magnetic orientation. (c) Plot of the average Fe L<sub>3</sub> spectra of all the parallel (red) or anti-parallel (blue) magnetosomes, along with the derived X-ray magnetic circular dichroism (XMCD), as points. The solid lines are the spectra and XMCD reported for synthetic magnetite (Goering *et al.* 2007), scaled to match the optical density. The reference XMCD spectra was divided by 2 since at 30° tilt angle only 0.5 of the magnetic moment is projected on to the photon spin vector.

**Figure 5** (a) Fe map of the 8 h sample from batch A from difference of OD images at 709.2 and 700 eV. The rectangles identify precursor (green), intermediate (cyan) and fully formed (red & blue) magnetosomes. (b) XAS spectra recorded with CR of regions identified in (a), plotted on an absolute OD scale without offsets. (c) rescaled and offset plots of the same data, compared to the Fe L<sub>3</sub> spectra of FeCl<sub>3</sub> and the spectra of magnetite recorded with parallel and antiparallel circular polarization (Goering et al 2007). When dots and lines are superimposed (middle chain, precursor chain), the dots are the experimental data while the solid lines are a smoothed version as a ‘guide to the eye’. The other solid lines correspond to unsmoothed experimental data and reference spectra. The good agreement of the spectrum of the big magnetosome with the anti-parallel spectrum of magnetite and that of the left chain with that of the parallel spectrum of magnetite shows that the magnetization vector of the big magnetosome and that of the left chain are oriented in opposite directions. The feature at 708.4 eV is strongest in the precursor chain (green) but is weak or absent in the other two chains, indicating a transition from Fe(III) to pure magnetite.

1  
2  
3  
4  
5  
6  
7  
8  
9  
10  
11  
12  
13  
14  
15  
16  
17  
18  
19  
20  
21  
22  
23  
24  
25  
26  
27  
28  
29  
30  
31  
32  
33  
34  
35  
36  
37  
38  
39  
40  
41  
42  
43  
44  
45  
46  
47  
48  
49  
50  
51  
52  
53  
54  
55  
56  
57  
58  
59  
60  
61  
62  
63  
64  
65

**Figure 6** Analysis of a cell from 5.7 h sample, batch B. (a,b) TEM images measured after the STXM measurements. (c) Average of all images of the Fe L<sub>3</sub> stack measured with CR with the sample at a tilt angle of 0°. (d) XMCD map (OD<sub>708.2</sub>-CR - OD<sub>708.2</sub>-CL) measured with the sample at a tilt angle of 0°. (e) XMCD map (OD<sub>708.2</sub>-CR - OD<sub>708.2</sub>-CL) measured with the sample at a tilt angle of 30°. (f) Fe L<sub>3</sub> XAS and XMCD spectra of all the black particles in Fig. 5e, measured with the sample at a tilt angle of 30°.

**Figure 7** Fe L<sub>3</sub> spectra extracted from an Fe L<sub>3</sub> stack of the 24 h AMB-1 sample from batch B, measured with CR at a tilt angle of 30°. These five spectra were used to fit the stack, so as to obtain the component maps presented in Figure 8.

**Figure 8** 24 h sample from batch B, measured with the sample plate tilted at 30°. (a) image of complete cell at 709.7 eV. (b) average of all 60 images of stack recorded in the top half of the cell. Component maps derived from a 5-component fit of the Fe L<sub>3</sub> image sequence (spectra shown in Fig. 7) of (c) cell, (d) Fe(III), (e) magnetosomes with antiparallel spectra in CR, (f) magnetosomes with parallel spectra in CR, (g) ‘rim’ signal, showing a band of Fe-containing material along the outer boundaries of the expanded part of the cell (bright in Fig. 8c). This spectral component also maps signals in the magnetosome chain. See Fig. S-5 for results of an alternate fit. (h) color coded composite of maps of the antiparallel (red), cell (green) and parallel (blue) component maps.

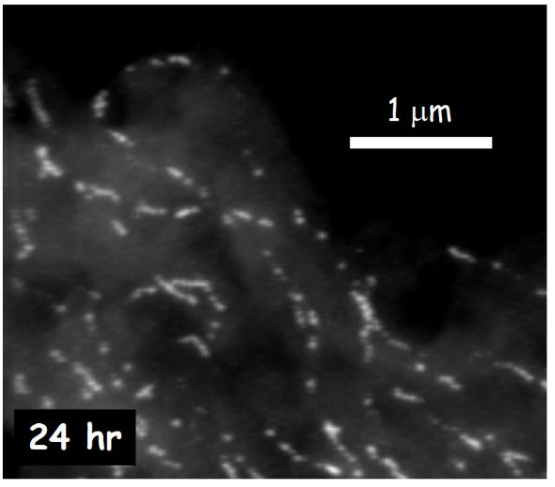
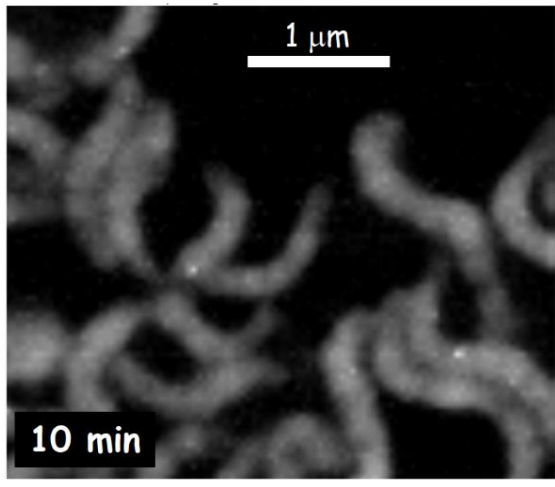
**Figure 9** Fe L<sub>3</sub> spectra of the magnetosomes in the 24 h AMB-1 cell of batch B recorded with CR and CL with the sample tilted at 30°. The resulting XMCD signal is also plotted. In each case the data from the magnetosomes of the cell from the 24 h sample is overplot with the corresponding spectra from pure magnetite (Goering et al, 2007).



1  
2  
3  
4  
5  
6  
7  
8  
9  
10  
11  
12  
13  
14  
15  
16  
17  
18  
19  
20  
21  
22  
23  
24  
25  
26  
27  
28  
29  
30  
31  
32  
33  
34  
35  
36  
37  
38  
39  
40  
41  
42  
43  
44  
45  
46  
47  
48  
49  
50  
51  
52  
53  
54  
55  
56  
57  
58  
59  
60  
61  
62  
63  
64  
65

865 **Graphical Abstract**

866



867

Figure 01  
[Click here to download high resolution image](#)

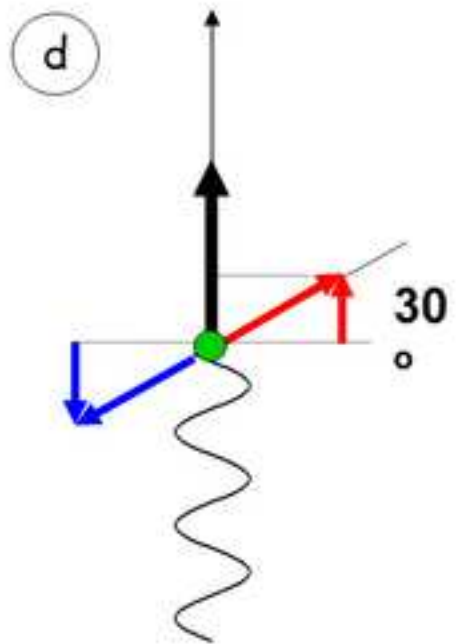
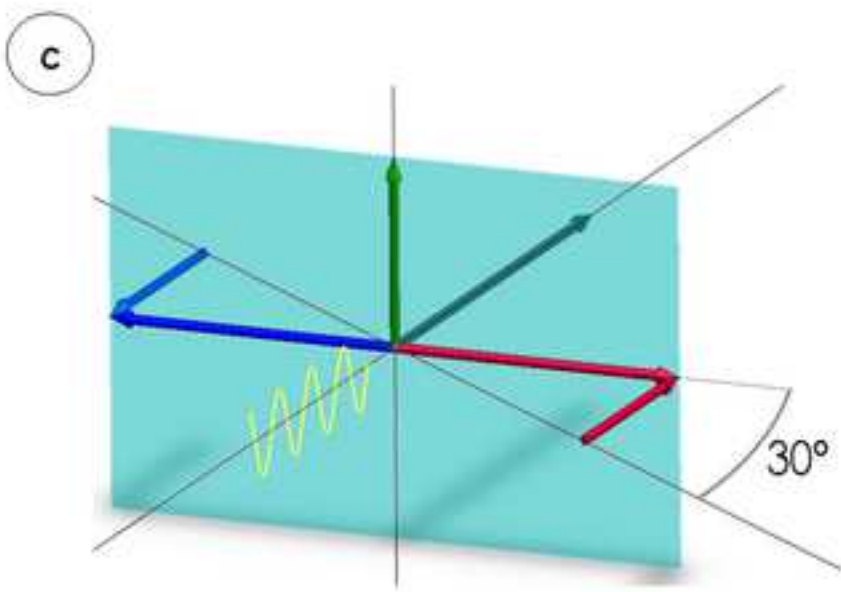
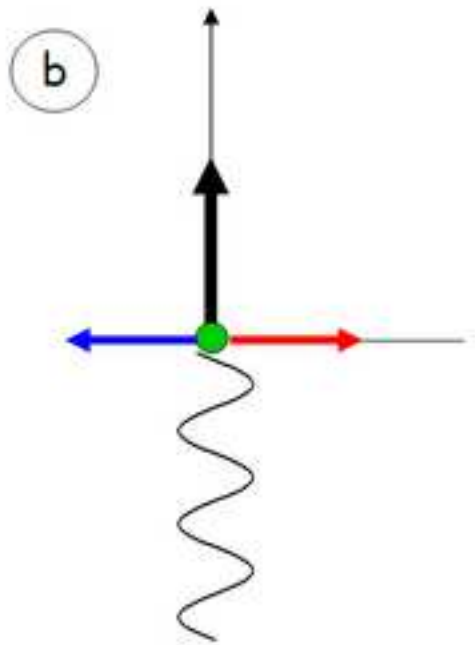
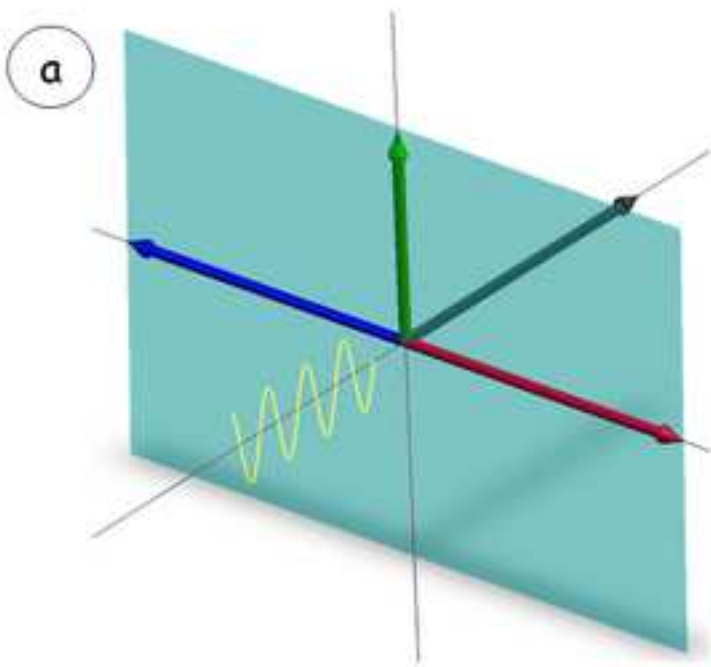


Figure 02  
[Click here to download high resolution image](#)

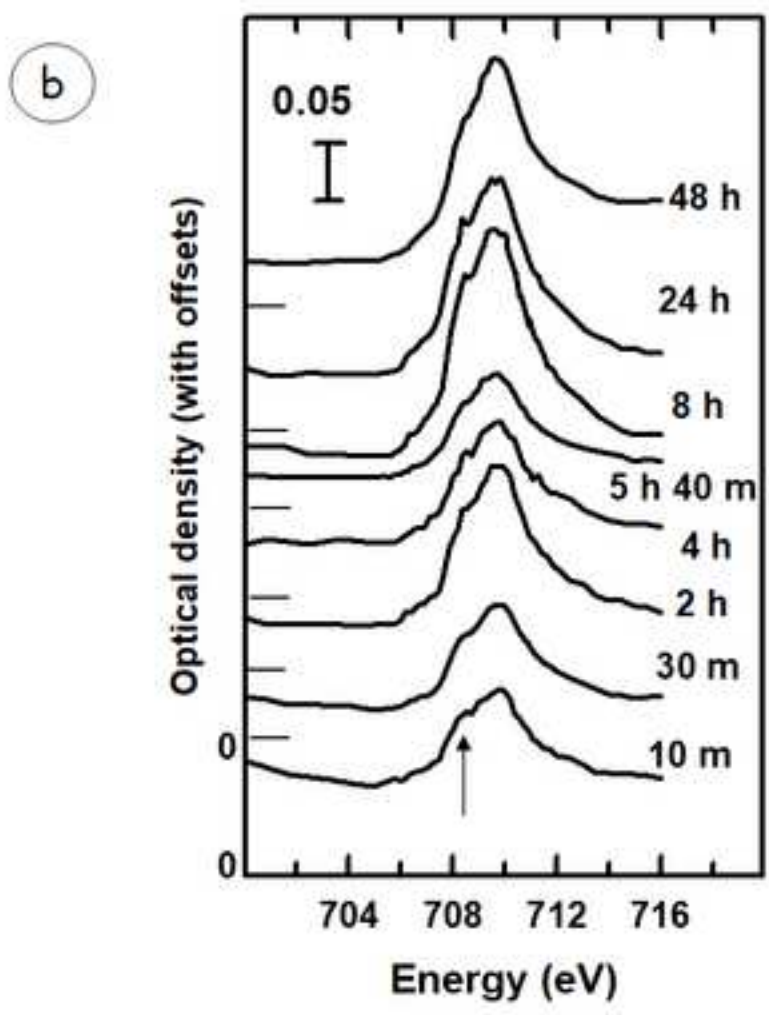
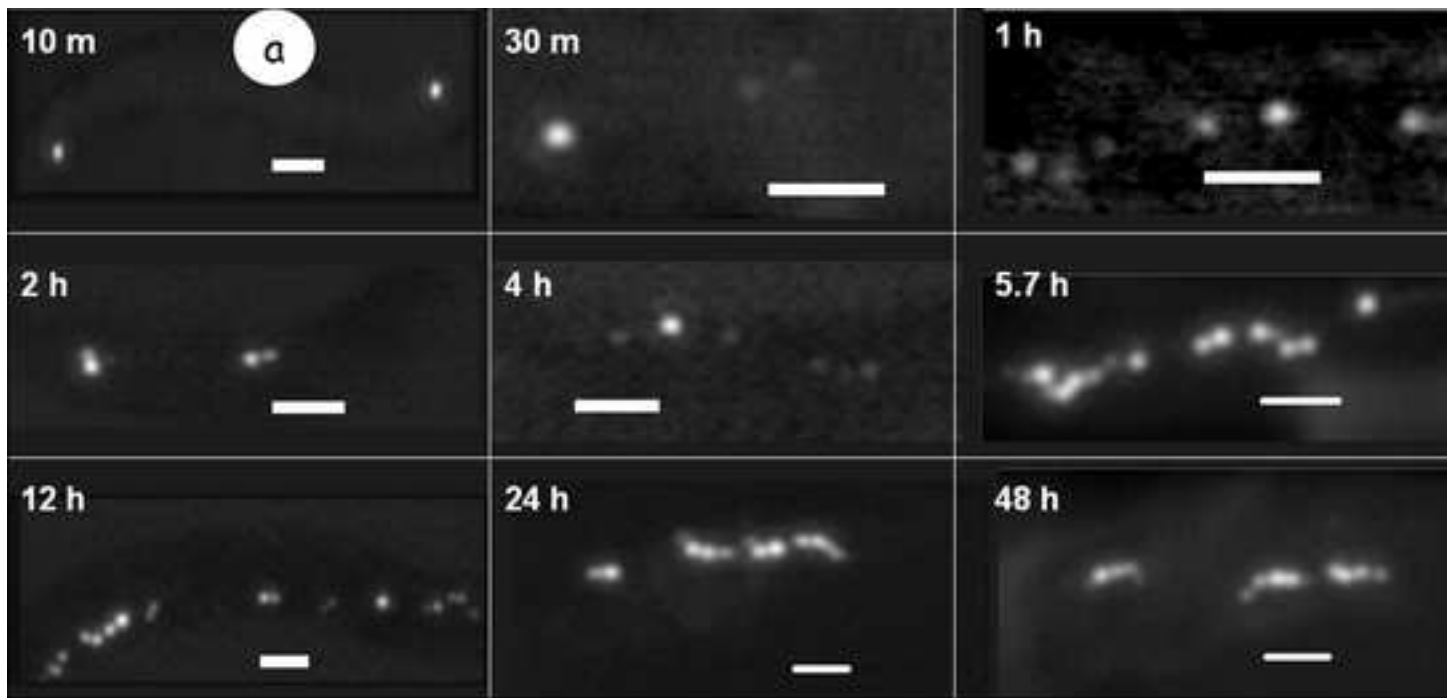


Figure 03

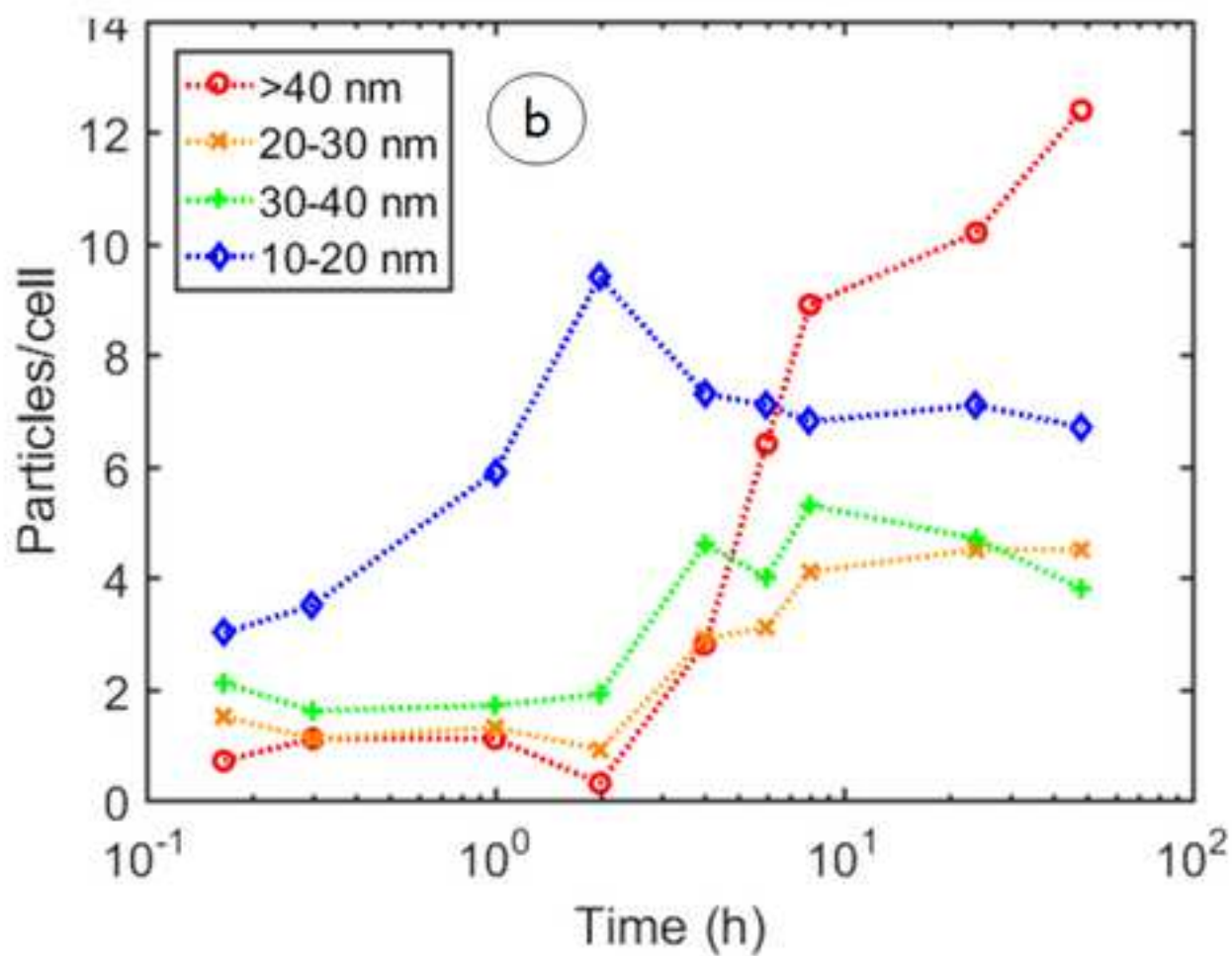
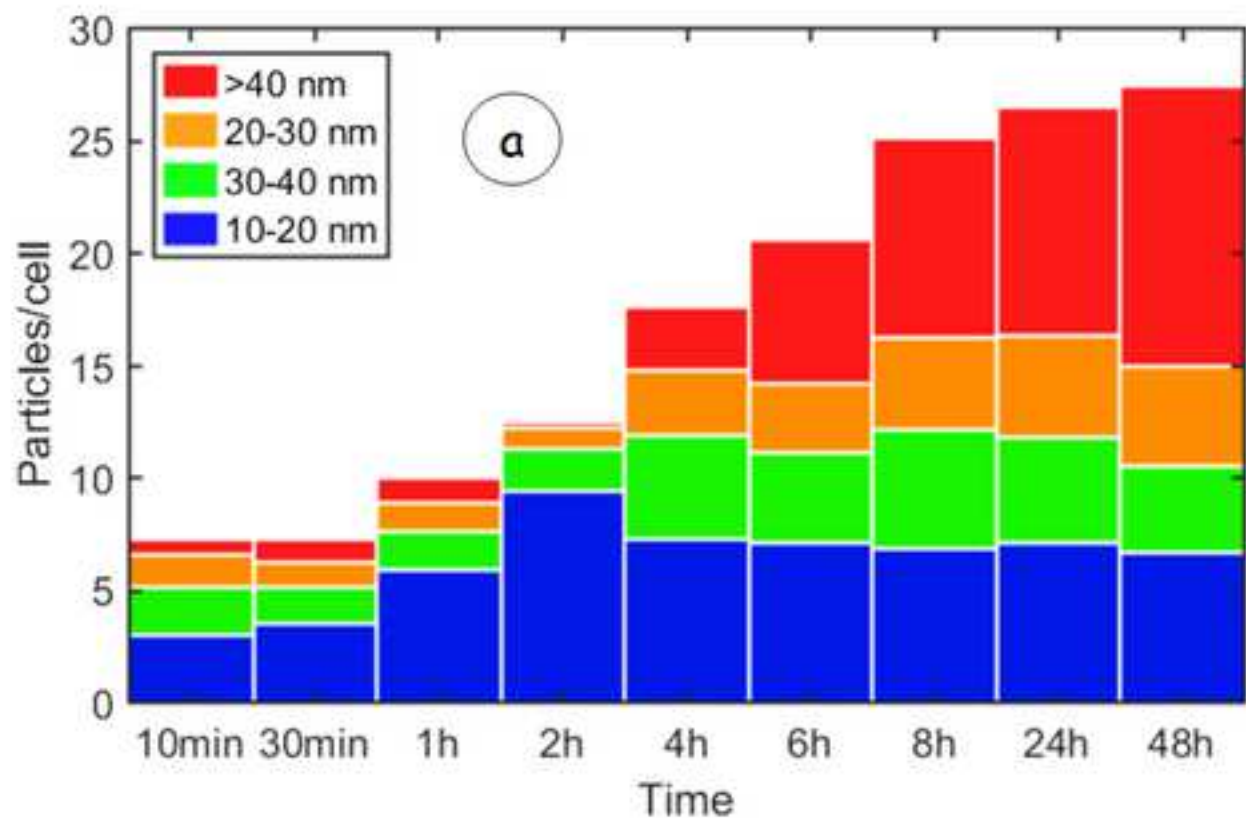
[Click here to download high resolution image](#)

Figure 04

[Click here to download high resolution image](#)

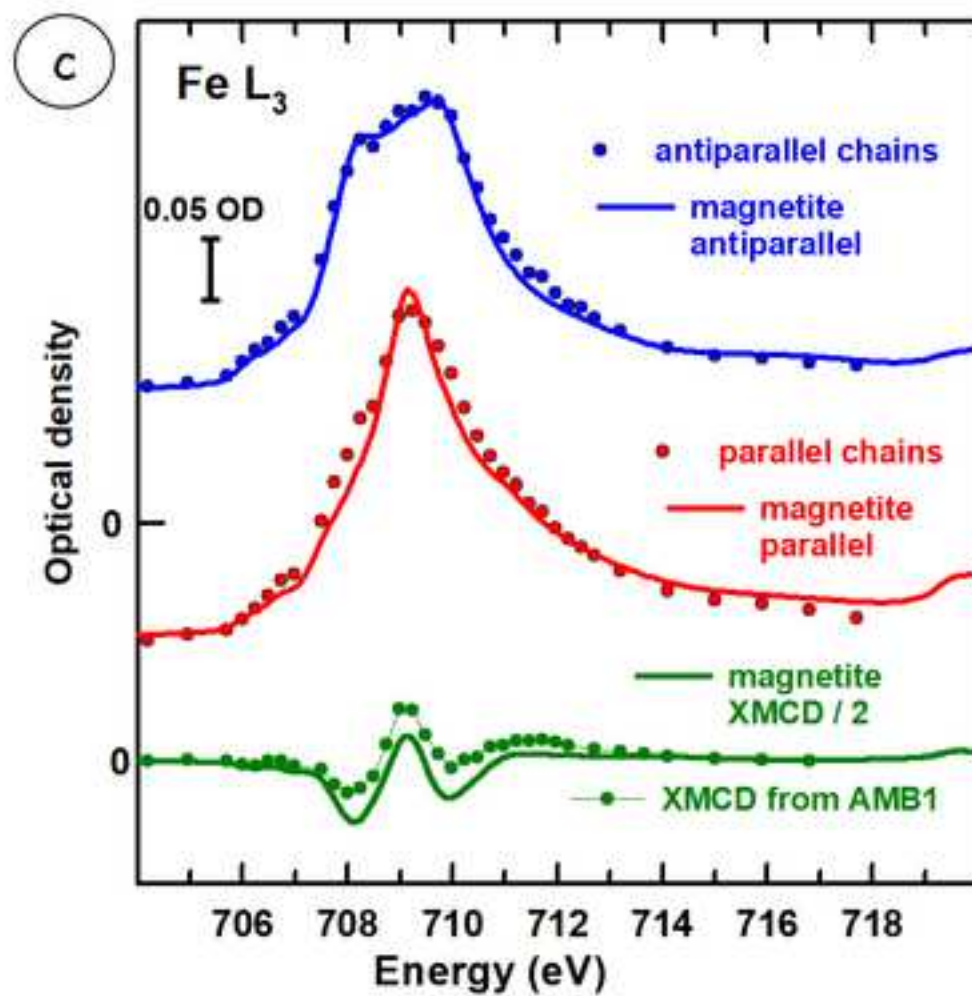
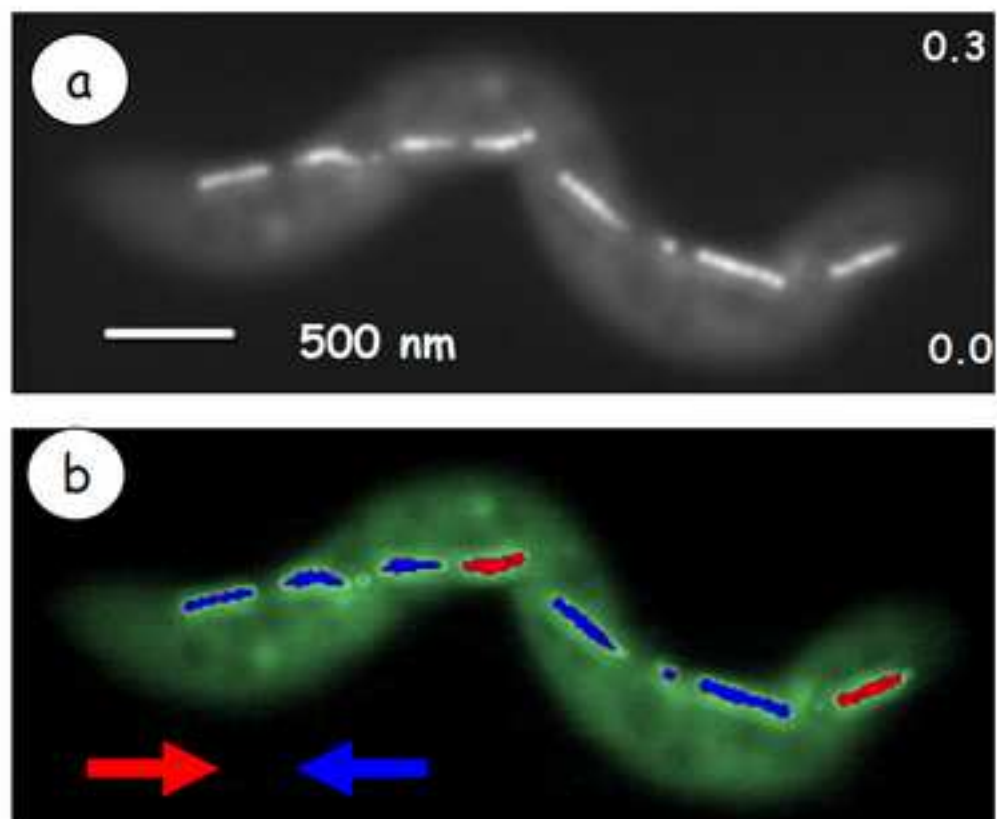


Figure 05

[Click here to download high resolution image](#)

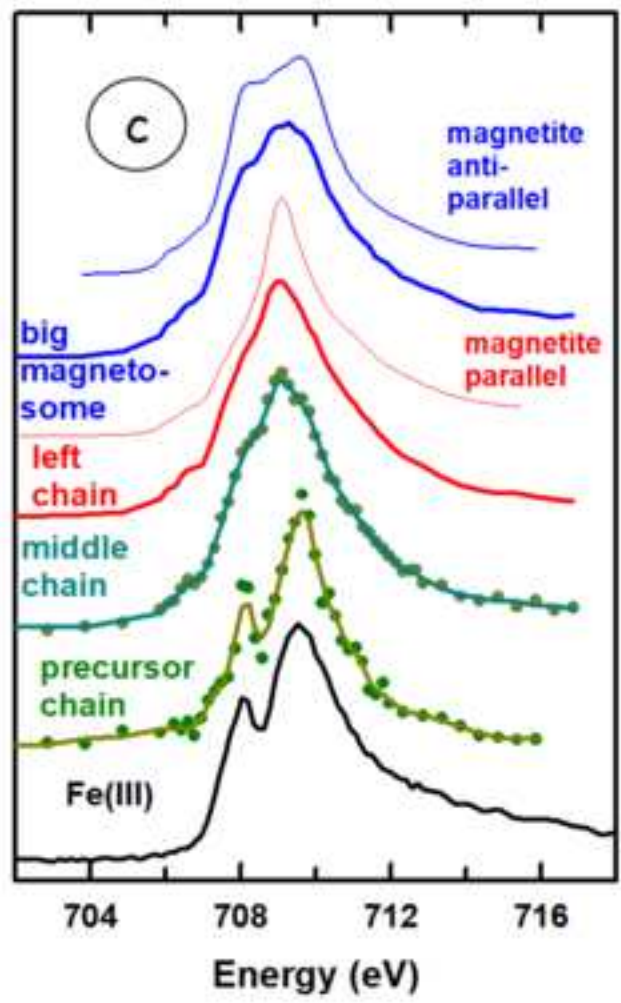
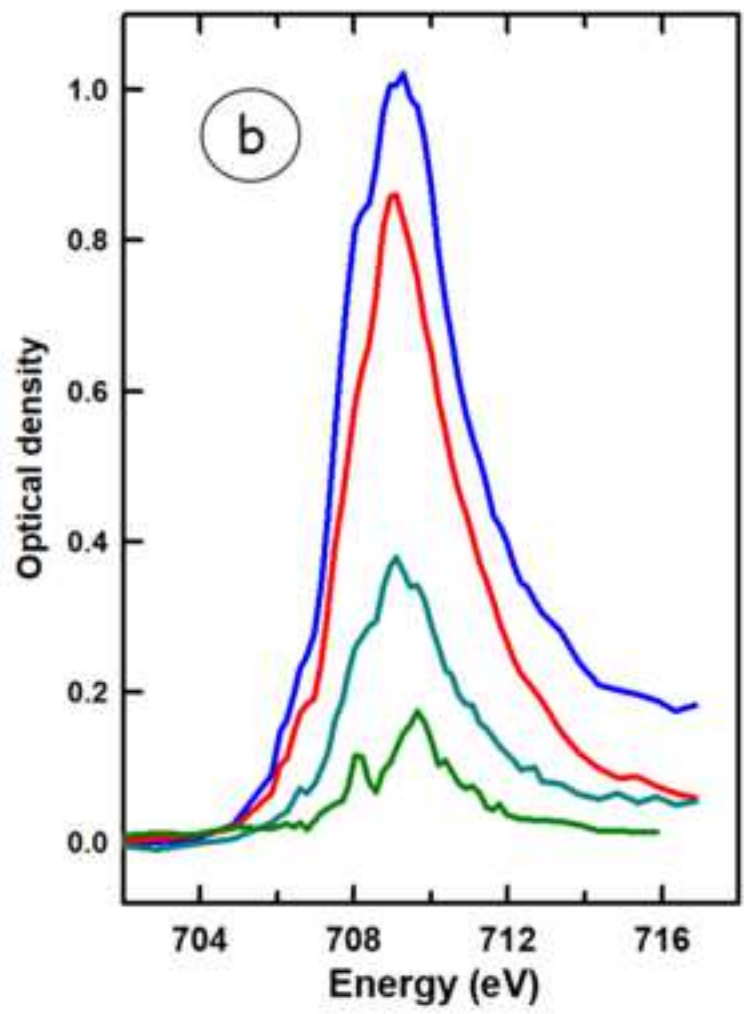
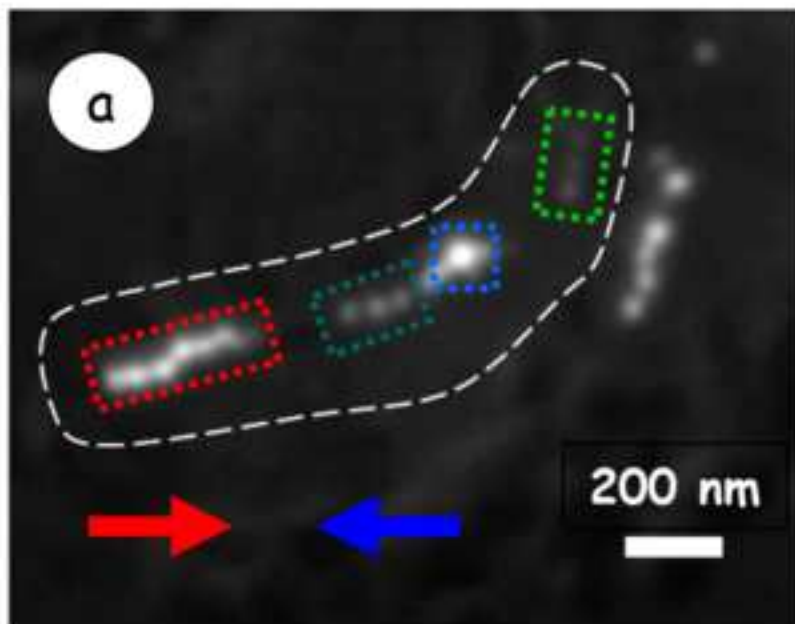


Figure 06

[Click here to download high resolution image](#)

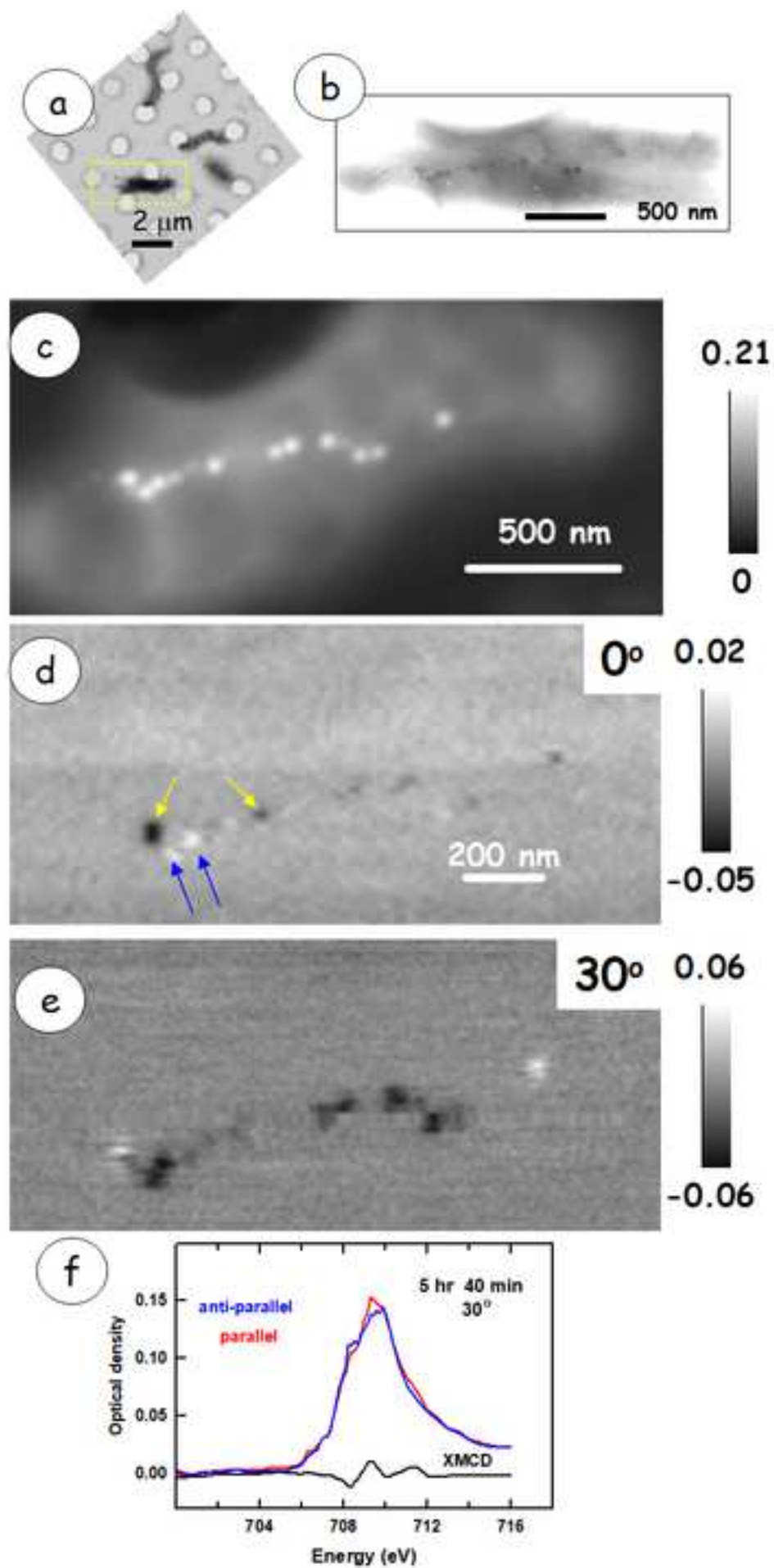


Figure 07  
[Click here to download high resolution image](#)

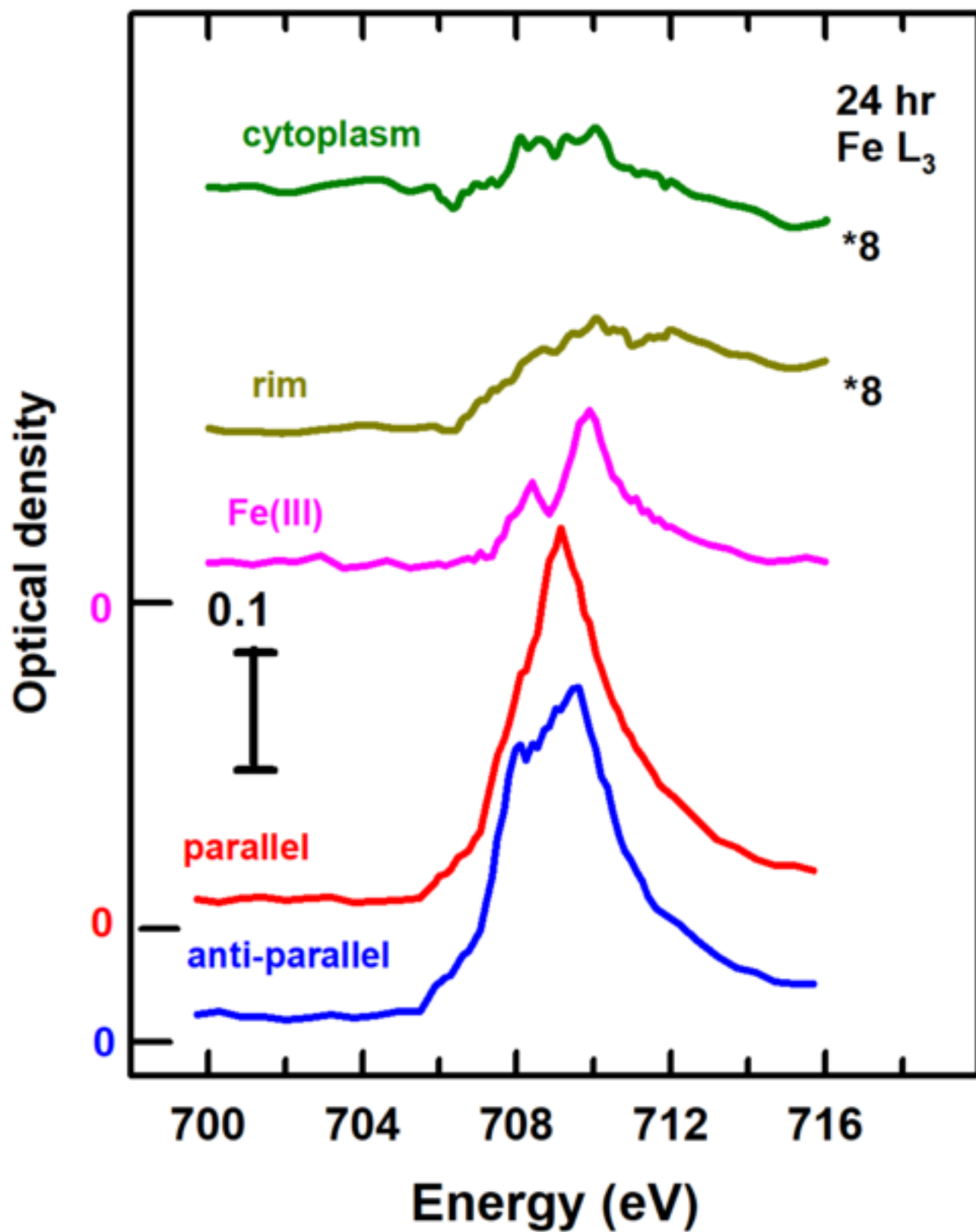




Figure 08

[Click here to download high resolution image](#)

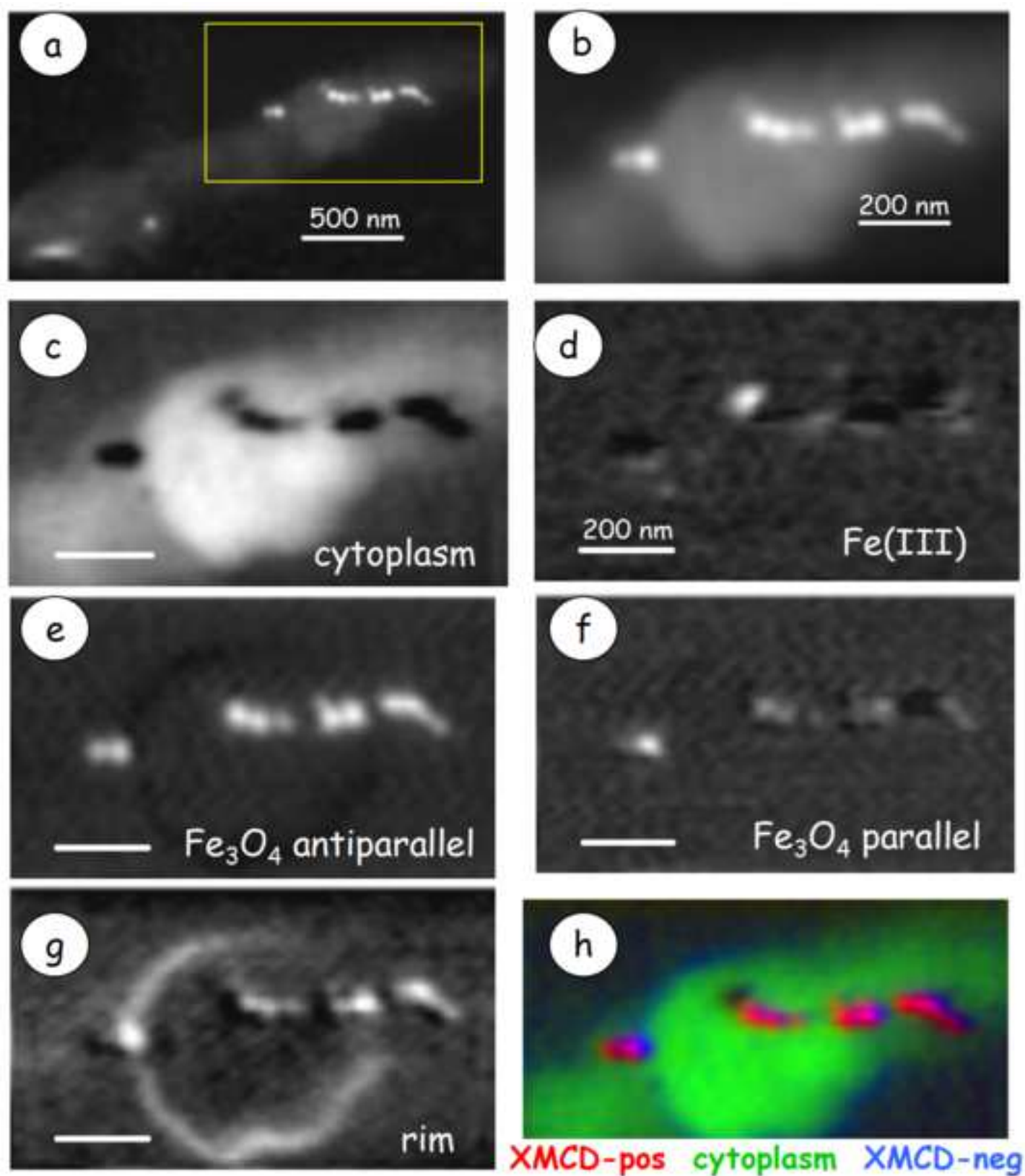
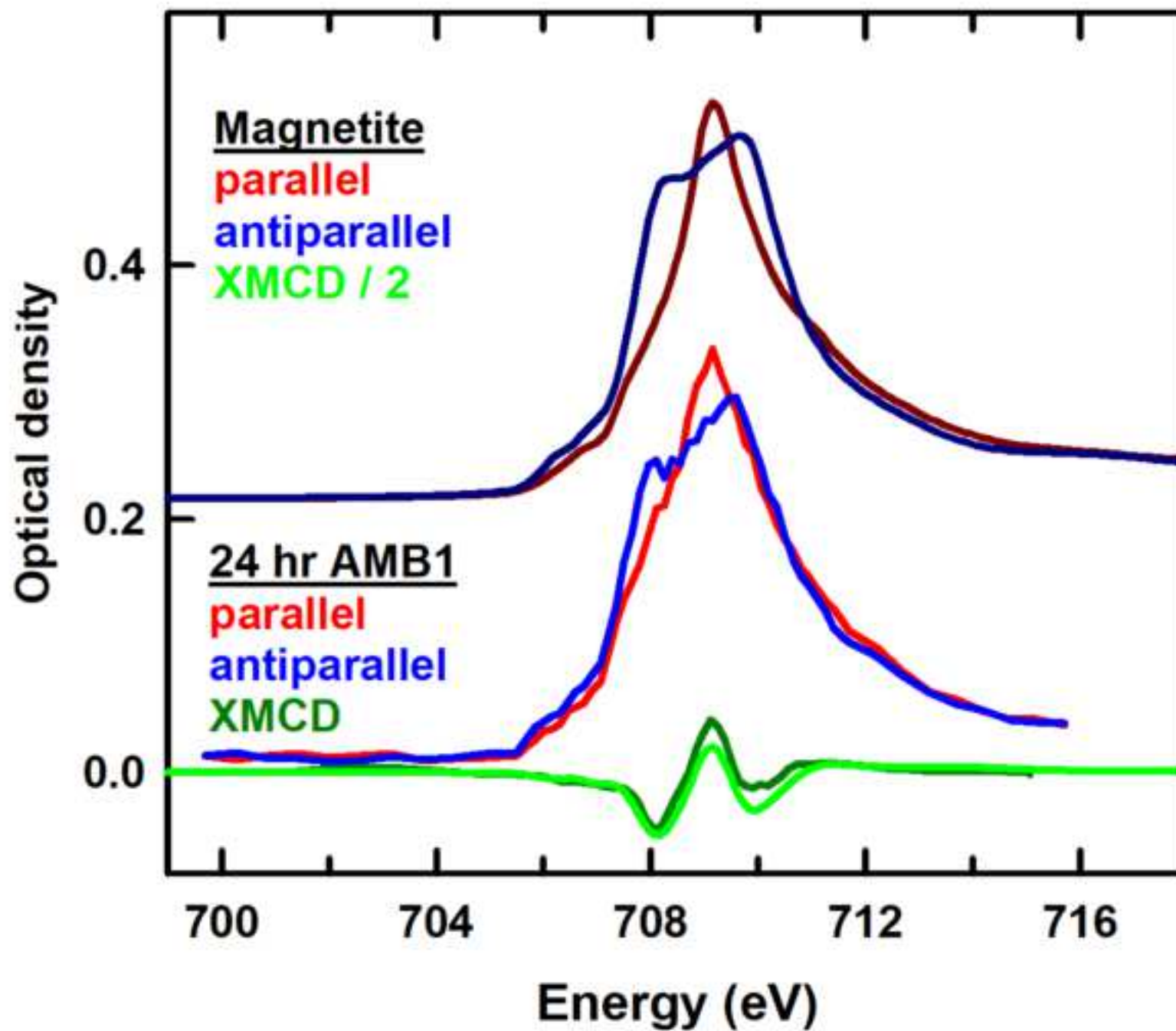


Figure 09

[Click here to download high resolution image](#)



**Supplementary information file**

[Click here to download Background dataset for online publication only: AMB1-time-course-STXM-SI-revised-submitted.pdf](#)